A&A 665, A60 (2022)
https://doi.org/10.1051/0004-6361/202243105
© D. N. Hoang et al. 2022

Astronomy & Astrophysics

Diffuse radio emission from non-*Planck* galaxy clusters in the LoTSS-DR2 fields

D. N. Hoang[1], M. Brüggen[1], A. Botteon[2], T. W. Shimwell[3,2], X. Zhang[2,4], A. Bonafede[5,6], L. Bruno[6,5], E. Bonnassieux[5], R. Cassano[6], V. Cuciti[1,6], A. Drabent[7], F. de Gasperin[1,6], F. Gastaldello[8], G. Di Gennaro[1], M. Hoeft[7], A. Jones[1], G. V. Pignataro[5,6], H. J. A. Röttgering[2], A. Simionescu[4,2,9], and R. J. van Weeren[2]

[1] Hamburger Sternwarte, Universität Hamburg, Gojenbergsweg 112, 21029 Hamburg, Germany
e-mail: hoang@hs.uni-hamburg.de
[2] Leiden Observatory, Leiden University, PO Box 9513, 2300 RA, Leiden, The Netherlands
[3] Netherlands Institute for Radio Astronomy (ASTRON), PO Box 2, 7990 AA Dwingeloo, The Netherlands
[4] SRON Netherlands Institute for Space Research, Niels Bohrweg 4, 2333 CA Leiden, The Netherlands
[5] Dipartimento di Fisica e Astronomia, Universitä di Bologna, via Gobetti 93/2, 40122 Bologna, Italy
[6] INAF – Istituto di Radioastronomia di Bologna, Via Gobetti 101, 40129 Bologna, Italy
[7] Thüringer Landessternwarte, Sternwarte 5, 07778 Tautenburg, Germany
[8] INAF – IASF Milano, via A. Corti 12, 20133 Milano, Italy
[9] Kavli Institute for the Physics and Mathematics of the Universe (WPI), The University of Tokyo, Kashiwa, Chiba 277-8583, Japan

Received 13 January 2022 / Accepted 31 May 2022

ABSTRACT

Context. The presence of large-scale magnetic fields and ultra-relativistic electrons in the intra-cluster medium (ICM) is confirmed through the detection of diffuse radio synchrotron sources, so-called radio halos and relics. Due to their steep-spectrum nature, these sources are rarely detected at frequencies above a few gigahertz, especially in low-mass systems.
Aims. The aim of this study is to discover and characterise diffuse radio sources in low-mass galaxy clusters in order to understand their origin and their scaling with host cluster properties.
Methods. We searched for cluster-scale radio emission from low-mass galaxy clusters in the Low Frequency Array (LOFAR) Two-metre Sky Survey – Data Release 2 (LoTSS-DR2) fields. We made use of existing optical (Abell, DESI, WHL) and X-ray (comPRASS, MCXC) catalogues. The LoTSS-DR2 data were processed further to improve the quality of the images that are used to detect and characterise diffuse sources.
Results. We detect diffuse radio emission in 28 galaxy clusters. The numbers of confirmed (candidates) halos and relics are six (seven) and 10 (three), respectively. Among these, 11 halos and 10 relics, including candidates, are newly discovered by LOFAR. In addition to these, five diffuse sources are detected in tailed radio galaxies and are probably associated with mergers during the formation of the host clusters. We are unable to classify a further 13 diffuse sources. We compare our newly detected, diffuse sources to known sources by placing them on the scaling relation between the radio power and the mass of the host clusters.

Key words. galaxies: clusters: general – galaxies: clusters: intracluster medium – large-scale structure of Universe – radiation mechanisms: non-thermal – X-rays: galaxies: clusters

1. Introduction

To date large-scale (∼megaparsec) radio emission has been primarily detected in dynamically disturbed, massive clusters of galaxies. These synchrotron sources trace the distribution of relativistic electrons and magnetic fields on cluster scales. The short lifetime of the radio-emitting relativistic electrons (10−100 Myr in a typical cluster environment) implies that they are locally (re-)accelerated throughout the intra-cluster medium (ICM) volume. Depending on location, size, morphology, and spectro-polarimetric properties, the diffuse radio sources in clusters are often classified as halos or relics. The different classes have been linked to different origins of the wide-scale and in situ particle acceleration (van Weeren et al. 2019, for a review).

Radio halos are megaparsec(Mpc)-scale, steep-spectrum[1] ($\alpha \lesssim -1$), unpolarised sources with a morphology that approximately follows thermal X-ray emission from the ICM. Clusters hosting radio halos are predominantly dynamically disturbed systems, indicating a connection between the formation of halos and the dynamical state (e.g., Cassano et al. 2010). The observed fraction of clusters with radio halos increases with cluster mass and is as high as 70 percent for the most massive systems ($M_{500} > 8\times10^{14}\,M_{\odot}$; Cuciti et al. 2015, 2021). Approximately 30 percent of radio halos are found in X-ray-luminous ($L_{0.1-2.4\,\mathrm{keV}} > 5\times10^{44}\,\mathrm{erg\,s^{-1}}$), nearby ($0.2 < z < 0.4$) clusters (Venturi et al. 2008; Kale et al. 2013). The synchrotron power of radio halos correlates with several other cluster properties, such as the cluster mass, the X-ray luminosity, and the Sunyaev-Zeldovich (SZ) signal (e.g., Liang et al. 2000; Brunetti et al. 2009; Basu 2012; Cassano et al. 2013; Sommer & Basu 2014; Cuciti et al. 2021).

Two main models have been proposed to explain the formation of radio halos: a turbulent re-acceleration scenario and models based on secondary electrons (see Brunetti & Jones 2014,

[1] The radio spectrum is defined as $S \propto \nu^{\alpha}$, where S is the source flux density at the frequency ν and α is the spectral index.

Open Access article, published by EDP Sciences, under the terms of the Creative Commons Attribution License (https://creativecommons.org/licenses/by/4.0), which permits unrestricted use, distribution, and reproduction in any medium, provided the original work is properly cited.
This article is published in open access under the Subscribe-to-Open model. Subscribe to A&A to support open access publication.

for a review). In the turbulent re-acceleration scenario, radio halos trace turbulent regions in the ICM where radio-emitting particles are re-accelerated by multi-scale turbulence during cluster-merger events (Brunetti et al. 2001; Petrosian 2001; Brunetti & Lazarian 2007). In the *secondary* model, relativistic electrons and gamma rays are generated as secondary products of inelastic collisions between relativistic protons and thermal ions that permeate the ICM. The re-acceleration model is supported by observational evidence, including the detection of ultra-steep spectrum radio halos (USSRHs; Brunetti et al. 2008), the presence of radio halos only in merging clusters (e.g., Cassano et al. 2013), and the absence of gamma rays from the Coma cluster (Brunetti et al. 2012, 2017; Ackermann et al. 2016). A combination of the two processes, where turbulence re-accelerates both *primary* and *secondary* electrons, can still be possible as this hybrid model can produce fainter gamma-ray emission that is below the detection limit of current observations (Brunetti et al. 2004; Brunetti & Lazarian 2011; Zandanel et al. 2014; Pinzke et al. 2017).

Radio relics are Mpc-sized, elongated, steep-spectrum ($\alpha \lesssim -1$) sources that are found in the peripheral regions of merging clusters. Some relics are highly polarised (up to 70 percent; e.g., van Weeren et al. 2010; Di Gennaro et al. 2021; Rajpurohit et al. 2021; de Gasperin et al. 2022). Observational evidence including X-ray surface brightness (SB) discontinuity and/or temperature jumps at the locations of radio relics supports the connection between the formation of relics and merger shocks (e.g., van Weeren et al. 2016a; Pearce et al. 2017). This connection is further supported by (*i*) the presence of polarised radio emission at shock fronts, which implies the alignment of the shock-compressed magnetic fields, and (*ii*) the observed steepening of radio spectral index in the regions behind the shocks due to the synchrotron and inverse-Compton (IC) losses. However, the origin of the relativistic particles emitting the synchrotron emission in relics has not been fully understood. For instance, it is unclear whether the relativistic particles are accelerated via Fermi-I diffusive shock acceleration from the thermal pool (DSA; Ensslin et al. 1997; Roettiger et al. 1999) or are re-accelerated via a DSA-like process from a mildly relativistic population of pre-existing relativistic electrons (Markevitch et al. 2005; Kang & Ryu 2011; Kang et al. 2012).

The diffuse radio sources in clusters (i.e. halos, relics) are characterised by steep ($\alpha \lesssim -1$) synchrotron spectra, which make them brighter at low frequencies. The LOFAR Two-metre Sky Survey (LoTSS; Shimwell et al. 2017) is a survey of the entire northern sky and was designed to produce radio maps at ∼6″ resolution between 120 and 168 MHz with ∼100 μJy beam^{-1} sensitivity noise level. This survey has enabled the discovery of new diffuse radio sources in clusters as well as the study of large samples of sources. Using the LoTSS first data release (LoTSS-DR1; Shimwell et al. 2019), van Weeren et al. (2021) studied the diffuse emission in 41 galaxy clusters located in the 424 deg^2 of the HETDEX Spring region. More recently, Botteon et al. (2022) analysed all the galaxy clusters reported in the second catalogue of SZ-detected sources (PSZ2; Planck Collaboration XXVII 2016) within the 5634 deg^2 area covered by the LoTSS – Second Data Release (LoTSS-DR2; Shimwell et al. 2022). Botteon et al. (2022) found that among the 309 galaxy clusters selected from the PSZ2 catalogue with $0.016 < z < 0.9$ and $1.1 \times 10^{14}\,M_\odot < M_{500} < 11.7 \times 10^{14}\,M_\odot$, 83 clusters host a radio halo and 26 clusters host one or more radio relics (including candidates). These two studies focused on the PSZ2 clusters, which effectively constitute a mass-selected sample that opens the possibility to perform statistical studies (Cassano et al., in prep.; Cuciti et al., in prep.; Jones et al., in prep.).

In this paper, we present our search for radio diffuse emission in galaxy clusters that are missed by these studies (i.e. van Weeren et al. 2021; Botteon et al. 2022) in non-PSZ2 clusters in the LoTSS-DR2 area. As the SZ signal is proportional to the mass of the ICM gas (e.g., Bender et al. 2016), the galaxy clusters that are not detected with the PSZ2 observations are likely to be low-mass systems. Cluster-scale radio sources in low-mass clusters are particularly interesting because theoretical models predict that the occurrence of the diffuse radio sources depends strongly on the mass of the host clusters (e.g., De Gasperin et al. 2014; Brüggen & Vazza 2020; Cassano et al. 2013). Thus, the presence of diffuse radio sources in low-mass clusters is crucial to constrain the models in this regime poorly explored by current observations.

Throughout this paper, we adopt a flat ΛCMD (Lambda cold dark matter) cosmology with $H_0 = 70\,\mathrm{km\,s^{-1}\,Mpc^{-1}}$, $\Omega_\mathrm{m} = 0.3$ and $\Omega_\Lambda = 0.7$. The images are plotted in the J2000 coordinate system.

2. The cluster sample

We visually inspected the images covered by the LoTSS-DR2 area spanning 5635 square degrees (Shimwell et al. 2022) to search for cluster-scale emission in the galaxy clusters that are detected with optical, X-ray, and SZ observations. To this end, we made use of optical (i.e. Abell: Abell et al. 1989; DESI: Zou et al. 2021; WHL: Wen et al. 2012; Wen & Han 2015), X-ray (i.e. MCXC: Piffaretti et al. 2011) and X-ray–SZ (i.e. comPRASS: Tarrío et al. 2019) cluster catalogues. In Table 1, we present a list of 28 galaxy clusters hosting cluster-scale radio emission in the LoTSS-DR2 images. In Fig. 1, we show the location of the clusters in our sample in the LoTSS fields. Throughout the paper, we assume that the centres of the galaxy clusters are the coordinates given in the respective catalogues, and they are reproduced in Table 1.

We note that our sample by no means represents a complete sample of the non-PSZ2 clusters hosting cluster-scale radio emission in the LoTSS-DR2 fields. These clusters with diffuse radio emission span masses between $M_{500} = 0.58 \times 10^{14} M_\odot$ and $8.14 \times 10^{14} M_\odot$, with a median of $2.83 \times 10^{14} M_\odot$. Our study therefore represents a first attempt to extend the sample of diffuse radio sources to clusters of lower masses (i.e. $\lesssim 2 \times 10^{14}\,M_\odot$). We note that the cluster masses M_{500} presented in this paper are obtained from multi-wavelength (optical, X-ray, SZ) catalogues and are not derived from weak lensing analyses. Hence, M_{500} here should be considered as mass proxies.

3. Data reduction

3.1. Calibration

LoTSS datasets for each pointing are calibrated for direction-independent (DI) and direction-dependent (DD) effects using the automatic standard pipelines `PREFACTOR`[2] (van Weeren et al. 2016b; Williams et al. 2016; de Gasperin et al. 2019) and `ddf – pipeline`[3] (Tasse et al. 2021), respectively. The pipelines are developed for the calibration of the Surveys Key Science Projects (SKSP) data. For details of the data processing of the LoTSS-DR2 data, we refer to Shimwell et al. (2022).

To improve the image fidelity towards the target direction, we follow the 'extraction' and self-calibration procedure that post-processes the archived `ddf – pipeline` products and is

[2] https://github.com/lofar-astron/prefactor
[3] https://github.com/mhardcastle/ddf-pipeline

Table 1. A sample of non-PSZ2 galaxy clusters that host diffuse sources in the LoTSS-DR2 fields.

No.	Name	RA [deg]	Dec [deg]	z	R_{500} [Mpc]	M_{500} [$\times 10^{14}\,M_\odot$]	$M_{500}^{\rm scaled}$ [$\times 10^{14}\,M_\odot$]	Scale [kpc/′]	X-ray	Ref.
1	Abell 84	10.4794	21.3771	0.102	0.96 ± 0.02	2.88 ± 0.43	2.86 ± 0.41	114	R	A89, W15
2	Abell 373	40.8613	27.9950	0.149	–	–	–	157	R	A89, G00
3	Abell 1213	169.1211	29.2603	0.048	–	–	–	57	X	A89, W98
4	Abell 1330	174.5984	49.5231	0.278	1.13	5.80 [(b)]	5.54	253	–	A89, W15
5	Abell 1889	214.1619	30.7358	0.185	0.91 ± 0.05	2.58 ± 0.39	2.58 ± 0.37	189	C[(a)], R	A89, W15
6	Abell 1943	219.4128	30.2341	0.336	1.31	8.70 [(b)]	8.14	289	–	A89, W15
7	Abell 1963	221.2036	31.4731	0.210	1.10	4.40 [(b)]	4.27	206	–	S99, W15
8	DESI 201	213.3731	43.9794	0.344	0.57 ± 0.04	0.77 ± 0.16	0.82 ± 0.16	297	–	Z21
9	DESI 296	138.2320	41.9373	0.155	0.55 ± 0.04	0.56 ± 0.12	0.61 ± 0.12	163	X	Z21
10	MCXC J0928.6+3747	142.1570	37.7990	0.247	0.95	3.15	3.90	236	R	P11
11	MCXC J0943.1+4659	145.7790	46.9980	0.406	0.97	3.97	4.75	330	X	P11
12	MCXC J1020.5+3922	155.1270	39.3800	0.143	0.47	0.33	0.58	152	–	P11
13	MCXC J1711.0+3941	257.7620	39.6940	0.065	0.70	1.02	1.50	76	R	P11
14	PSZRX G095.27+48.27	230.8676	59.8819	0.362	–	3.23	3.34	307	–	T19
15	PSZRX G100.21-30.38	350.5707	28.5264	0.388	–	5.71	5.77	320	X	T19
16	PSZRX G102.17+48.88	223.7294	62.9749	0.292	–	3.13	3.25	266	–	T19
17	PSZRX G116.06+80.14	194.3289	36.9139	0.518	–	6.74	6.76	378	X[(a)], R	T19
18	PSZRX G181.53+21.43	110.3160	36.7426	0.175	–	2.28	2.40	180	R	T19
19	PSZRX G195.91+62.83	162.0091	31.6423	0.515	–	5.55	5.62	378	–	T19
20	WHL J002056.4+221752	5.2352	22.2977	0.199	0.60	0.86 [(b)]	0.96	200	R	W15
21	WHL J002311.7+251510	5.7987	25.2527	0.109	0.75	1.38 [(b)]	1.46	121	–	W15
22	WHL J085608.5+541855	134.0355	54.3152	0.251	–	2.93 [(b)]	2.80	238	R	W15
23	WHL J091721.4+524607	139.3391	52.7685	0.192	–	4.10 [(b)]	3.76	194	–	W15
24	WHL J101350.8+344251	153.4616	34.7142	0.146	–	2.56 [(b)]	2.49	155	–	W15
25	WHL J130503.5+314255	196.2644	31.7153	0.396	0.90	3.52 [(b)]	3.29	325	–	W15
26	WHL J165540.4+334422	253.9183	33.7394	0.255	0.72	1.25 [(b)]	1.33	241	–	W15
27	WHL J172125.4+294144	260.3557	29.6957	0.184	–	2.32 [(b)]	2.29	187	–	W15
28	WHL J173424.0+332526	263.5999	33.4239	0.485	0.60	1.26 [(b)]	1.34	366	–	W15

Notes. Column 1: cluster number in the sample. Column 2: cluster name. Column 3: Right Ascension (J2000). Column 4: Declination (J2000). Column 5: cluster redshift. Column W15: the radius enclosing the cluster volume at which the mean over-density is 500 times the critical density of the Universe at the cluster redshift. Column 7: cluster mass within R_{500}. Column 8: cluster mass that is scaled to that of the PSZ2 clusters (see Sec. 5.2). Column 9: angular scale at the cluster redshift. Column 10: available X-ray data. Available X-ray data is denoted as C for *Chandra*, X for *XMM-Newton*, and R for ROSAT. Column 11: reference. A89: Abell et al. (1989), G00: Gal et al. (2000), P11: Piffaretti et al. (2011), S99: Struble & Rood (1999), T19: Tarrío et al. (2019), W98: Wu et al. (1998), W15: Wen & Han (2015), Z21: Zou et al. (2021). [(a)]Proprietary data. [(b)]M_{500} is derived using the M_{500}-richness scaling relation (Eq. (17) in Wen & Han 2015).

described in van Weeren et al. (2021) and Botteon et al. (2022). To maximise the signal-to-noise ratio (S/N) of the detected sources, we include all the data from LoTSS-DR2 pointings that are centred within 2.2° from the target cluster. Within this radius, the sensitivity of the primary beam is at least 50 percent of that at the pointing centre. The extracted regions covering the targets are typically 0.3–0.7 deg^2 in size and within this region the primary beam response is assumed to be constant. Finally, multiple self-calibration loops including phase and phase-amplitude are performed. For details, we refer to van Weeren et al. (2021) and Botteon et al. (2022).

3.2. Imaging and source subtraction

In order to search for cluster-scale emission, we follow the imaging procedure for the PSZ2 clusters in Botteon et al. (2022) to obtain images of our targets at several different angular resolutions using `WSClean`[4] (version 2.10.0). To alter the resolution, we image with a Briggs' weighting robust parameter of −0.5 without and with a tapering of outer baselines (i.e. `taper-gaussian`) with two-dimensional Gaussian functions of 10″, 15″, 30″, and 60″ FWHM (full-width at half maximum). For our datasets, this typically corresponds to resolutions of 8″, 19″, 25″, 38″, and 74″, respectively. The `uv` data below 80 $k\lambda$ are not used in the imaging as they are generally more contaminated with radio frequency interference (RFI) and we do not require the very large-scale emission that they offer sensitivity to. For instance, these short baselines map diffuse emission with angular scales of larger than 53′, which corresponds to physical scales that are larger than 11 Mpc at $z = 0.19$ (i.e. the redshift median for our sample) or 3 Mpc for the nearest cluster of galaxies (i.e. Abell 1213 at $z = 0.048$) in the sample. To accurately deconvolve faint diffuse emission across the full bandwidth, the deconvolution is performed with the multiscale with a multifrequency cleaning algorithm. We split the bandwidth of 48 MHz into six narrower sub-bands which are jointly deconvolved (i.e. `join-channels` and `channels-out=6`) and we deconvolve with scales (i.e. `multiscale-scales`) of $[0, 4, 8, 16, 32, 64]$ in units of pixels, where the zero corresponds to a delta function for modelling of point sources.

Diffuse radio emission from the ICM is often contaminated by the emission from individual radio galaxies that are located in the clusters or along the line of sight. We remove the contamination from the discrete sources by subtracting their models from the *uv* data. These models are created by imaging with a Briggs' weighting robust parameter of −0.5 and by cutting the shortest baselines in order to remove large-scale cluster emission that extends beyond physical scales of 250 kpc. The *uv*-data are then used to make images at multiple resolutions with identical settings to those made prior to source subtraction.

[4] https://gitlab.com/aroffringa/wsclean

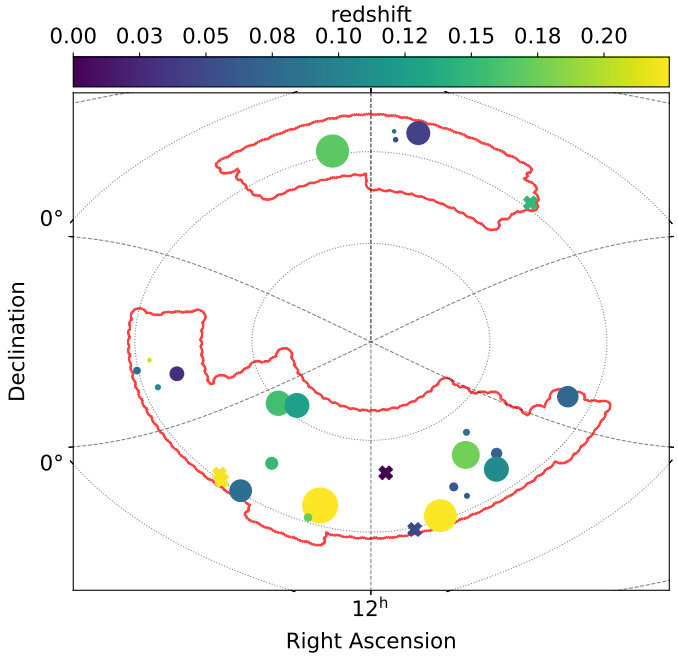

Fig. 1. Location of the clusters in the LoTSS-DR2 fields shown with the red lines. The colour code presents the redshift of the clusters. The size of the points indicates the relative mass of the cluster, M_{500}. Clusters without M_{500} are shown with crosses.

3.3. Flux-scale correction

The flux scale of the LoTSS-DR2 *uv*-data is calibrated according to Scaife & Heald (2012) using the bookended observations of 3C radio sources (e.g., 3C 196, 3C 295). The calibration does not take into account errors of the LOFAR beam model. As a result, radio sources across the LOFAR wide-field images have non-uniform uncertainties in their flux densities depending on their relative location with respect to the centre of the grid pointings. Another source of uncertainty in the integrated flux densities of radio sources comes from phase calibration errors. The phase errors scatter flux and can systematically impact the measured values. To assess and partially correct these, Shimwell et al. (2022) align the flux scale of the LoTSS-DR2 mosaics and catalogue with the Roger et al. (1973) flux scale through a comparison with 6C and the NRAO Very Large Array Sky Survey (NVSS; see also Hardcastle et al. 2021).

Following Botteon et al. (2022), we align the flux scale of our LOFAR images with the LoTSS-DR2 catalogue which gives us comparable errors to that catalogue. The scaling factors for each cluster field are obtained by comparing the integrated flux densities of the compact sources in our images (i.e. those with robust of −0.5 without tapering of outer baselines) with those in the LoTSS-DR2 catalogue. A linear relation between the flux densities is fitted using three techniques including Theil-Sen (Sen 1968), Huber (Huber 1981), and traditional linear regressions that are built in the `scikit-learn` package[5]. The different fitting procedures are used because they have different outlier rejection criteria and for each field we use the fitting method that has the lowest mean absolute error. To align the flux scale, our LOFAR images are multiplied by the scaling factors. For our sample, the scaling factors range between 0.7 and 1.2, with the mean value of 1.0 and a standard deviation of 0.1. In this paper, we adopt a flux scale uncertainty of 10 percent which is consistent with variations in the LoTSS-DR2 flux density scale (Shimwell et al. 2022).

3.4. Flux density and power measurements

We measure the flux density of diffuse cluster sources by integrating over those pixels that are above 2σ, that is, the region where the pixel values are more than twice the root mean square (RMS) of the local background noise (σ) and within a manually defined region that is shown with the cyan dashed lines in the corresponding figures (e.g., see Fig. 2 for Abell 84). In cases where diffuse cluster emission is contaminated by the emission from discrete sources, we identify the contaminated regions by eye and manually mask out the emission; these regions are shown with black dashed lines. We account for this missing flux density in the masked regions by extrapolating the measured diffuse cluster emission flux density using the area ratio between the masked and unmasked ($>2\sigma$) regions. The uncertainty in the flux density is estimated as follows,

$$\Delta S = \sqrt{N \times \sigma^2 + (f_{\rm err} \times S)^2 + (e_{\rm mask} \times S_{\rm mask})^2}, \quad (1)$$

where N is the area of diffuse sources in beam units; σ (Jy beam^{-1}) is the RMS of the background noise; $f_{\rm err}$ is the flux scale uncertainty (i.e. assuming 10 percent); S (Jy) is the integrated flux density of the diffuse sources; $e_{\rm mask}$ and $S_{\rm mask}$ are the uncertainty, assuming 20 percent, and the extrapolated flux density for the masked region. Another source of uncertainty is due to the lack of short baselines (i.e. below 80 kλ), a subject that was extensively studied using simulations of radio halos by Bruno et al. (in prep.). These authors found that the flux density recovered by the LoTSS observations is more than 90 percent for halos with an angular size of smaller than 10.5′ (i.e. 2 Mpc at $z = 0.2$). As the real size of the halos in our sample is unknown, the estimates of the flux density we report in this paper do not include this type of uncertainty.

For detected and candidate radio halos, we additionally estimate the flux densities by fitting their SB profile with 2D models using the Halo-Flux Density CAlculator (`Halo-FDCA`) code[6] (Boxelaar et al. 2021). The SB profile of radio halos is modelled with an exponential function:

$$I(\mathbf{r}) = I_0 e^{-G(\mathbf{r})}, \quad (2)$$

where I_0 is the SB at the halo centre and $G(\mathbf{r})$ is the function that defines the morphology of the halos (e.g., circular, elliptical, or skewed). For the explicit mathematical form of the morphological function $G(\mathbf{r})$, we refer to Boxelaar et al. (2021). Depending on the models, the number of free parameters varies. For instance, the circular model has four free parameters describing the central brightness (I_0), the location (two for Right Ascension (RA) and Declination (Dec)), and the extension (e-folding radius). The elliptical model has two additional free parameters for the extension and the orientation of the fitted ellipsoid. The skewed model has two more free parameters compared to the elliptical model. The `Halo-FDCA` code uses a Markov chain Monte Carlo (MCMC) algorithm to search for the best-fit parameters and their uncertainties. Once the best-fit parameters are found, the flux densities of the halos can be integrated out to a radius defined by the user. In this study, we fit the SB of the detected and candidate halos with the circular, elliptical, and skewed models. The integrated flux density is calculated to a radius of three times the e-folding radius which is commonly used

[5] https://scikit-learn.org

[6] https://github.com/JortBox/Halo-FDCA

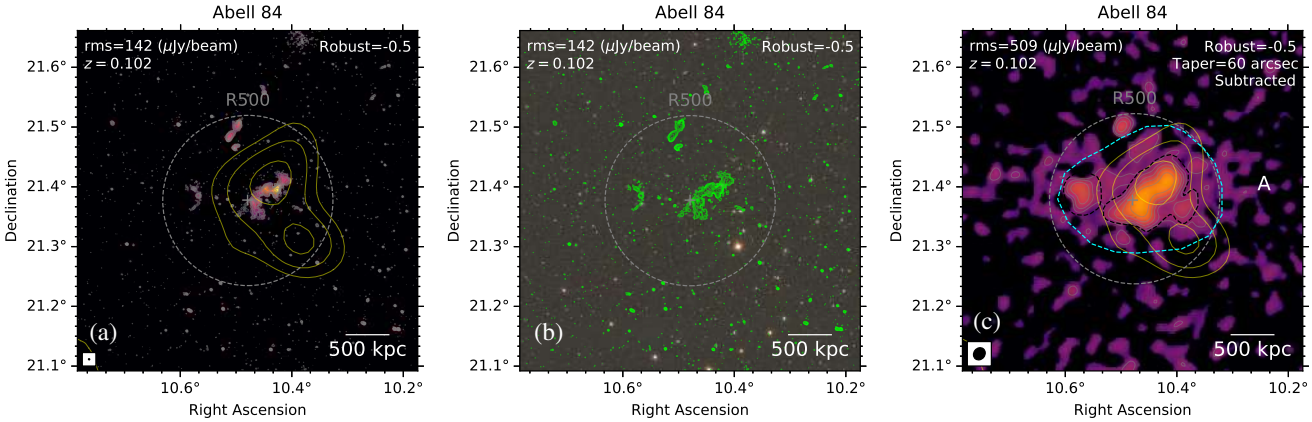

Fig. 2. Abell 84. LOFAR 144 MHz images (*a*, *c*) at different resolutions shown in the bottom-left corners. The optical SDSS image (*b*) is overlaid with the LOFAR contours. In all images, the LOFAR first contour is drawn at 3σ, where σ is shown in the top-left corners. The next contours are multiplied by a factor of 2. In panels *a* and *c*, the X-ray yellow contour is drawn at 3σ, and subsequently spaced by a factor of $\sqrt{2}$. In panel *c*, the cyan dashed line shows the region where source flux density is measured. The black dashed line region is masked out. All pixels below 2σ are blanked. The cluster centre is marked with the grey plus symbol. The grey dashed circle has a radius of R_{500}.

in literature (e.g., Murgia et al. 2009; van Weeren et al. 2021). We find that the models result in consistent flux density estimates within 1σ for all detected or candidate halos in our sample, which is consistent with the analysis in Botteon et al. (2022). Hence, we only report the flux densities obtained from the elliptical model in Table 2. The best-fit parameters are summarised in Appendix A.

The radio power of all diffuse cluster sources is estimated using the corresponding flux density estimates,

$$P = 4\pi D_L^2 \, K(z) \, S, \tag{3}$$

where D_L is the luminosity distance to the target; $K(z) = (1+z)^{-(1+\alpha)}$ is the standard radio k-correction term for a source at redshift z; here we assume a spectral index of $\alpha = -1.2$, which is commonly found for diffuse radio sources in galaxy clusters (e.g., Feretti et al. 2012; van Weeren et al. 2019).

3.5. Ancillary data

We make use of optical and X-ray archival data to assist with the identification of the diffuse radio sources and to characterise the dynamical status of the clusters. In the optical band, we make use of the *g*, *r*, and *i* filter images from the Sloan Digital Sky Survey (SDSS) survey (Alam et al. 2015). In the X-ray band, we find that only 13 (46 percent) of the clusters where we detect radio emission have been observed and are usable in the X-rays with *Chandra*, *XMM-Newton*, or ROSAT All Sky Survey (RASS; see Table 1). The *Chandra* and *XMM-Newton* X-ray data are calibrated in a similar manner to Botteon et al. (2022).

4. Results

In this section, we present LOFAR 144 MHz images and diffuse emission classifications making use of the multi-wavelength data of the galaxy clusters listed in Table 1. The multiple-resolution images show the presence of diffuse emission at different scales. In clusters where diffuse emission is co-located in projection with discrete sources, we remove these contaminating sources (see Sec. 3.2) and present the source-subtracted images, which are indicated with 'Subtracted' in the top right corner of the images. The classification and flux measurements for the diffuse sources in the cluster sample are presented in Table 2.

4.1. Abell 84

As seen in the LOFAR images in Fig. 2, multiple discrete radio sources are detected in the centre and outskirts (N and E) of the galaxy cluster Abell 84 ($z = 0.102$). In Fig. 2b, the central radio sources roughly follow the distribution of optical cluster galaxies, which is in line with the cluster galaxy number map presented in Strazzullo et al. (2005). In the low-resolution, source-subtracted image in Fig. 2c, faint diffuse emission is newly detected at 2σ around the central discrete sources and roughly follows the main part of the ROSAT X-ray emission. The projected size of the diffuse source is 1500 kpc × 740 kpc with the major axis in the E-W direction. Based on the location and the extension of the diffuse source, we classify it as a candidate radio halo. We estimate the flux density of the candidate halo by (i) integrating the $>2\sigma$ pixels within the cyan region (Fig. 2c) and (ii) fitting the SB with the elliptical model (see Sect. 3.4). The resulting estimates are given in Table 2.

4.2. Abell 373

In Fig. 3, LOFAR images show the new detection of diffuse radio sources in Abell 373 ($z = 0.149$), named A–C. About 1.1 Mpc to the NW of the cluster centre (as reported in the Abell catalogue), we detect a diffuse source (A) with a projected size of 770 kpc × 200 kpc elongated in the N-S direction. The southern part of source A is only seen in the low-resolution images in Fig. 3b,c. Source A has no optical counterpart in the SDSS image (see Fig. 3b). On the eastern side of the cluster, at 1.5 Mpc from source A, an elongated source (B) is detected in the low-resolution image in Fig. 3b. Source B is similar in projected size and orientation to source A. The morphology and location of A and B suggest that they are radio relics. Figure 3c shows the presence of a 800 kpc × 1000 kpc diffuse source (C) connecting sources A and B. Source C partly covers the ROSAT X-ray low-S/N emission. We classify source C as a radio halo. The 144 MHz flux densities of the sources A, B, and C are given in Table 2.

4.3. Abell 1213

Abell 1213 ($z = 0.048$, the lowest redshift in the sample) is a non-relaxed galaxy cluster hosting the brightest radio galaxy (BCG; 4C29.41) in the cluster centre (Jones & Forman 1999;

Table 2. Classification of cluster diffuse sources.

Cluster	Source	VC	DTC	RA [deg]	Dec [deg]	$S_{2\sigma}$ [mJy]	$P_{2\sigma}$ [$\times 10^{23}$ W Hz^{-1}]	$S_{\rm fit}$ [mJy]	$P_{\rm fit}$ [$\times 10^{23}$ W Hz^{-1}]	Size [kpc × kpc]
Abell 84	A	cH	H	10.4794	21.3771	91.9 ± 14.3	24.6 ± 3.8	131.9 ± 15.4	35.6 ± 4.2	1500 × 740
Abell 373	A	R	R	40.7516	28.0640	50.3 ± 5.2	30.8 ± 3.2	–	–	770 × 200
	B	R	R	40.9168	27.9990	27.6 ± 2.9	16.9 ± 1.8	–	–	770 × 200
	C	H	H	40.8332	28.0333	23.9 ± 3.3	14.6 ± 2.0	–	–	1000 × 800
Abell 1213	A	U	NDE	169.2839	29.3074	71.7 ± 7.3	3.9 ± 0.4	–	–	260 × 80
Abell 1330	A	cH	cH	174.5626	49.5312	13.7 ± 1.8	–	13.0 ± 1.9	–	–
Abell 1889	A	R	R	214.0442	30.8462	141.3 ± 14.6	142.1 ± 14.7	–	–	1650 × 830
	B	R	R	214.2344	30.6948	112.3 ± 11.7	112.9 ± 11.7	–	–	1650 × 570
Abell 1943	A	cR/Rem	cR	219.4436	30.1821	5.0 ± 0.7	7.8 ± 1.1	–	–	370 × 170
Abell 1963	A	cR/Rem	NDE	221.2542	31.5131	36.9 ± 3.8	55.2 ± 5.6	–	–	200 × 200
DESI 201	A	U	U	213.3675	43.9744	66.0 ± 6.7	278.0 ± 28.1	–	–	620 × 270
DESI 296	A	U	U	138.2187	41.9881	24.8 ± 2.6	16.7 ± 1.8	–	–	550 × 200
MCXC J0928.6+3747	A	R	R	142.1828	37.7782	35.2 ± 3.6	68.2 ± 7.0	–	–	350 × 250
	B	R	R	142.1169	37.7550	46.9 ± 4.7	90.8 ± 9.2	–	–	300 × 200
	C	H	H	142.1433	37.7846	68.1 ± 6.9	131.9 ± 13.4	88.7 ± 9.0	52.3 ± 10.3	850 × 400
MCXC J0943.1+4659	A	R	R	145.8396	47.0212	18.6 ± 2.0	116.7 ± 12.2	–	–	530 × 460
	B	H	H	145.7581	47.0013	56.0 ± 6.2	350.8 ± 38.6	70.8 ± 7.4	4.4 ± 1.4	1200 × 1200
MCXC J1020.5+3922	A	Rem	U	155.1381	39.3548	122.1 ± 12.4	68.8 ± 7.0	–	–	360 × 230
PSZRX G095.27+48.27	A	R	cR	230.9914	59.8315	50.1 ± 5.2	237.8 ± 24.4	–	–	1300 × 450
	B	cH	cH	230.8795	59.9022	20.4 ± 2.5	96.7 ± 12.1	–	–	1200 × 610
PSZRX G100.21-30.38	A	H	H	350.5623	28.5211	31.4 ± 3.6	175.7 ± 19.9	41.4 ± 4.9	232.0 ± 27.5	600 × 380
PSZRX G102.17+48.88	A	cH/Rem	cH	223.7520	62.9871	19.6 ± 2.0	56.0 ± 5.8	18.6 ± 2.0	53.0 ± 5.8	460 × 340
PSZRX G116.06+80.14	A	cH/Rem	U	194.3397	36.9133	4.4 ± 0.6	50.2 ± 7.0	–	–	340 × 250
PSZRX G181.53+21.43	A	R	R	110.4594	36.8719	91.8 ± 9.3	81.0 ± 8.2	–	–	1000 × 250
	B	U	NDE	110.2951	36.6618	300.2 ± 30.1	264.8 ± 26.5	–	–	600 × 300
	C	AGN	NDE	110.4509	36.5985	16.4 ± 2.0	14.5 ± 1.8	–	–	900 × 90
	D	cH	H	110.3850	36.7665	–	–	–	–	–
PSZRX G195.91+62.83	A	H	NDE	162.0178	31.6440	16.5 ± 1.8	185.2 ± 19.8	15.5 ± 1.8	173.0 ± 20.0	600 × 600
WHL J002056.4+221752	A	U	NDE	5.2696	22.3358	155.2 ± 15.8	183.1 ± 18.6	–	–	1000 × 1000
	B	U	NDE	5.2817	22.3614	84.3 ± 8.7	99.5 ± 10.2	–	–	1000 × 400
WHL J002311.7+251510	A	U	NDE	5.8322	25.2764	47.9 ± 4.9	15.0 ± 1.5	–	–	230 × 120
WHL J085608.5+541855	A	Rem	U	134.0545	54.2582	15.5 ± 1.6	31.0 ± 3.3	–	–	380 × 210
WHL J091721.4+524607	A	U	NDE	139.3118	52.7691	11.8 ± 2.0	12.8 ± 2.2	–	–	290 × 170
	B	AGN	NDE	139.3072	52.8599	6.1 ± 0.9	6.7 ± 1.0	–	–	350 × 170
WHL J101350.8+344251	A	R	cR	153.5143	34.6818	4.7 ± 0.7	2.8 ± 0.4	–	–	310 × 150
	B	U	NDE	153.4087	34.7283	7.1 ± 0.8	4.2 ± 0.5	–	–	220 × 140
	C	cH	cH	153.4531	34.7043	9.7 ± 1.1	5.7 ± 0.6	–	–	900 × 300
WHL J130503.5+314255	A	H	cH	196.2470	31.7164	22.9 ± 2.8	134.3 ± 16.7	19.7 ± 2.6	116.0 ± 15.4	1400 × 800
	B	cR	cR	196.3271	31.7141	2.8 ± 0.6	16.6 ± 3.5	–	–	1400 × 320
	C	U	cR	196.1985	31.7700	8.6 ± 1.0	50.3 ± 6.1	–	–	720 × 360
WHL J165540.4+334422	A	Rem	U	253.8790	33.7450	35.4 ± 3.7	73.3 ± 7.7	35.9 ± 3.9	74.6 ± 8.1	630 × 400
WHL J172125.4+294144	A	U	U	260.2237	29.7245	19.3 ± 2.3	19.0 ± 2.3	–	–	560 × 260
	B	R	cR	260.1413	29.7298	23.1 ± 2.8	22.8 ± 2.7	–	–	600 × 340
WHL J173424.0+332526	A	U	NDE	263.6228	33.4883	137.8 ± 13.8	1332.8 ± 133.7	–	–	800 × 330
	B	U	NDE	263.6175	33.4510	94.9 ± 9.6	917.6 ± 92.6	–	–	840 × 290

Notes. Column 1: cluster name. Column 2: source name. Column 3: visual classification (VC). Column 4: decision-tree classification (DTC; R: relic, H: halo, cR: candidate relic, cH: candidate halo, U: unclassified/uncertain, Rem: AGN remnant, NDE: no diffuse emission). Column 5: right ascension. Column 6: declination. Column 7: 144 MHz flux density measured within 2σ contour. Column 8: radio power estimated from $S_{2\sigma}$. Column 9: 144 MHz flux density obtained by fitting the SB profile with elliptical model. Column 10: radio power at 144 MHz estimated from $S_{\rm fit}$. Column 11: projected size of the source.

Fanti et al. 1982; Ledlow et al. 2003; Giovannini et al. 2009). VLA 1.4 GHz observations by Giovannini et al. (2009) show the detection of a diffuse source to the east of the BCG and these authors classified the source as a small-size radio halo. The power of the radio halo of Abell 1213 does not follow the correlation between radio halo power and X-ray luminosity (Giovannini et al. 2011).

In Fig. 4, LOFAR images confirm the presence of the central radio galaxy and the diffuse emission to the eastern region. The diffuse emission is connected with the central radio galaxy; its major axis follows the distribution of optical cluster galaxies; and its SB does not follow the distribution of X-ray emission (see Fig. 4). These suggest that the diffuse emission is not a radio halo, but is the tail of the central radio galaxy. We measure the projected size of the tailed galaxy to be 510 kpc. Interestingly, excess diffuse emission is detected in the easternmost region of the tail galaxy; this is what we refer to as source A. There are no obvious counterparts to source A seen in the SDSS image in Fig. 4b. The projected size of source A is 260 kpc × 80 kpc. Across source A, from the eastern direction, the SB increases rapidly towards the central region of the source, but the SB gradually decreases on the other side towards the cluster centre. The

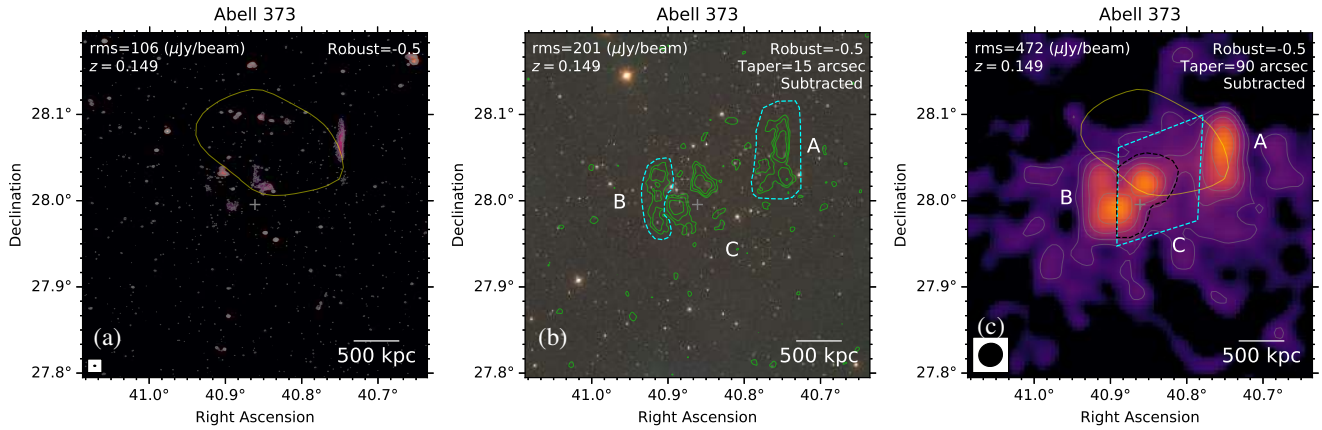

Fig. 3. Abell 373. Image description is the same as that in Fig. 2.

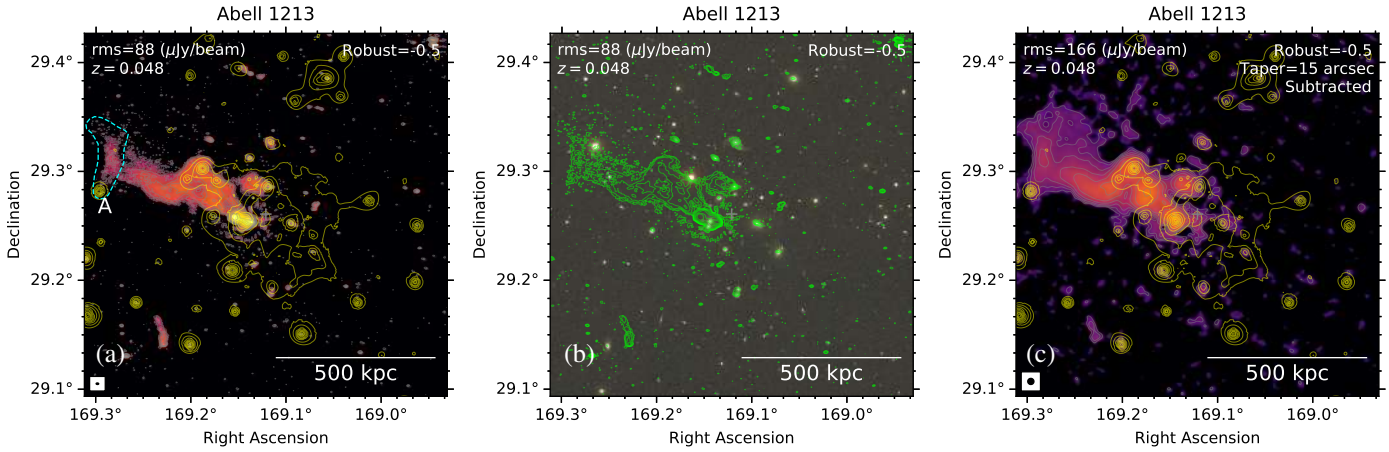

Fig. 4. Abell 1213. Image description is the same as that in Fig. 2.

origin of the excess emission (source A) is still unknown. It could be associated with a merger that is occurring in the NE-SW direction as suggested by the disturbed morphology of the *XMM-Newton* X-ray emission and the distribution of the optical cluster galaxies in Fig. 4.

4.4. Abell 1330

In Fig. 5 we present LOFAR images of Abell 1330. The high-resolution image in the left panel shows a high noise level around compact sources to the south of the cluster centre. There is no redshift information reported for this cluster in the literature. In panel c, the source-subtracted low-resolution image shows the new detection of a diffuse radio source that is not visible in the high-resolution image in panel a. The diffuse emission has a projected size of 3.5′ (i.e. 700 kpc if $z = 0.2$) and is located 1.5′ in the northwestern direction from the centre (as reported in Abell et al. 1989). Its SB follows the distribution of the galaxies in the SDSS image in panel b, and therefore we classify the diffuse source as a candidate radio halo. The 144 MHz flux density of the diffuse source is given in Table 2. Without redshift, we are not able to estimate the radio power of the source.

4.5. Abell 1889

LOFAR images of Abell 1889 ($z = 0.185$) in Fig. 6 show the new detection of two diffuse sources, named A and B for the NW and SE sources, respectively. These sources are located on the boundaries of the ROSAT X-ray emission and are on opposite sides (2.5 Mpc apart in projection) of the cluster centre. The projected sizes of these diffuse sources are roughly equal (i.e. 1650 kpc × 830 kpc and 1650 kpc × 570 kpc, respectively). The major axes of sources A and B are perpendicular to the line connecting the sources through the cluster centre. The brightness of source A increases along its length from NE to SW. The SB of source B is higher in the middle region. There are no clear optical counterparts for A and B seen in the SDSS optical image in panel b of Fig. 6. The morphology and location of sources A and B suggest that they are radio relics. We estimate the 144 MHz flux density and radio power of the relics and present them in Table 2. In the region between the relics, we find small-scale diffuse emission behind the relic A (see panel c), but we do not see large-scale emission connecting the relics where the ROSAT X-ray emission is detected.

4.6. Abell 1943

Figure 7 shows a number of tailed radio galaxies in the central region of Abell 1943 ($z = 0.225$) detected by LOFAR. The orientation of these radio galaxies shows that they are moving in different directions with respect to the ICM, indicating that the cluster is in a dynamically disturbed state. Southeast of the cluster centre, an elongated diffuse source with a projected size of 370 kpc × 170 kpc is newly detected in the low-resolution image

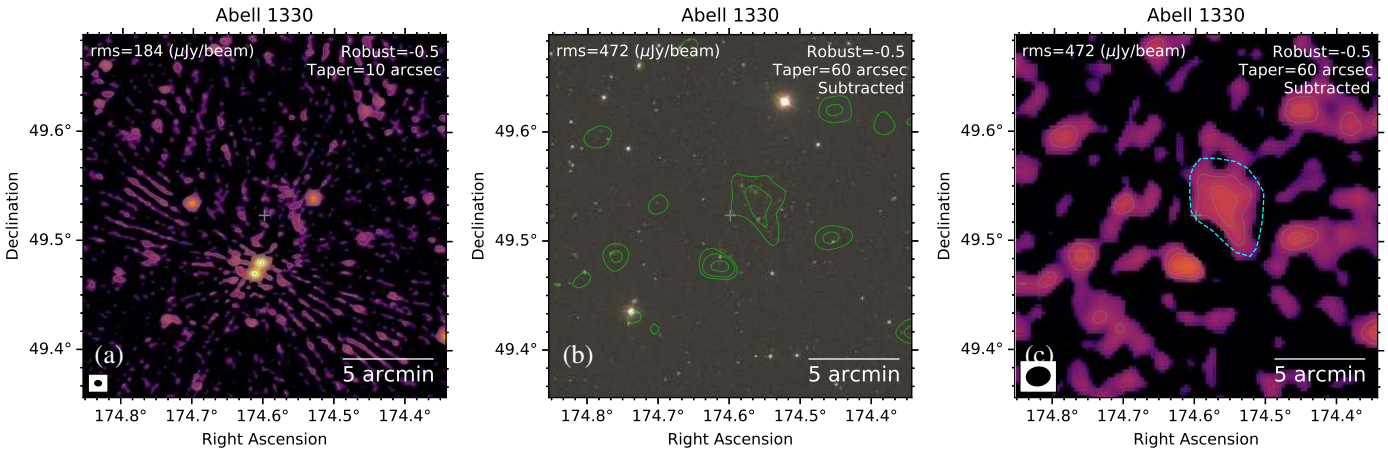

Fig. 5. Abell 1330. Image description is the same as that in Fig. 2.

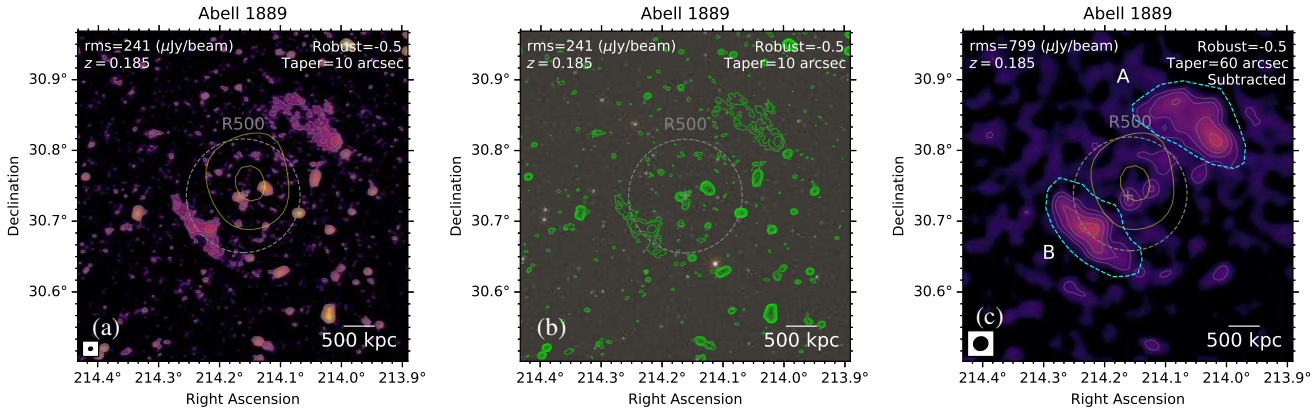

Fig. 6. Abell 1889. Image description is the same as that in Fig. 2.

(see panel c). No optical counterpart associated with the diffuse source is seen in the SDSS image in panel b. The flux density and power of the source at 144 MHz are given Table 2. The diffuse source could be a radio relic generated during the formation of the cluster or an active galactic nucleus (AGN) remnant.

4.7. Abell 1963

In Fig. 8, we present LOFAR and SDSS images of Abell 1963 (z = 0.221). The cluster galaxies in the SDSS image are distributed in the NE-SW direction, indicating that Abell 1963 is a dynamically disturbed system. The cluster centre is likely close to the location of the radio galaxies (i.e. RA = 221.2226°, Dec = 31.5031°), where most of the galaxies seen in the optical image reside, rather than that reported in the Abell catalogue (Abell et al. 1989). The LOFAR images show the detection of two tailed radio galaxies in the centre. At the end of the galaxy tails, a diffuse source, named source A, is newly detected. Source A has a projected size of 200 kpc and is connected with the radio galaxies through low-SB emission in its western direction. The diffuse source could be fossil plasma from radio galaxies or a radio relic generated during the formation of the cluster.

4.8. DESI 201

LOFAR images in Fig. 9 show the new detection of diffuse emission in DESI 201 (z = 0.344). The diffuse source has a projected size of 620 kpc × 270 kpc and has no SDSS optical counterpart. It could be associated with radio galaxies, but its true nature is still unknown.

4.9. DESI 296

LOFAR images displayed in Fig. 10 show the new detection of a diffuse source in DESI 296 (z = 0.155), named source A. The diffuse source with a projected size of 550 kpc × 200 kpc is located 500 kpc to the north of the cluster centre. The SDSS image in panel b shows no clear optical counterpart associated with source A. However, part of the radio emission to the northern and southern sides of source A is from individual galaxies as shown in the LOFAR high-resolution contours in panel b. The 144 MHz flux density and power of source A are given in Table 2. Source A is about 600 kpc from the central X-ray emission seen in panels a and c. The location and extension of source A are consistent with those for relics, but its morphology, bending towards the outer direction of the cluster, is unusual and the source does not show a typical SB profile (i.e. sharp edge in the outside) as seen in other relics. Additional high-frequency radio (polarimetric) observations will be needed to understand the nature of the source.

4.10. MCXC J0928.6+3747

MCXC J0928.6+3747 (z = 0.247; also known as Abell 800) was reported by Govoni et al. (2012) to host a diffuse radio source that they classified as a radio halo. Despite the classification, the

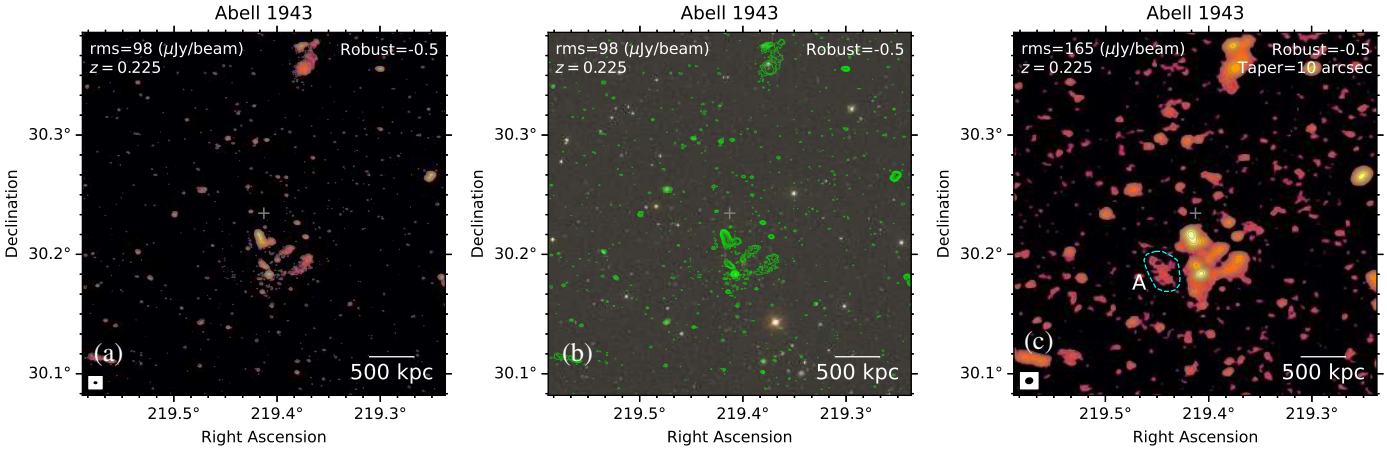

Fig. 7. Abell 1943. Image description is the same as that in Fig. 2.

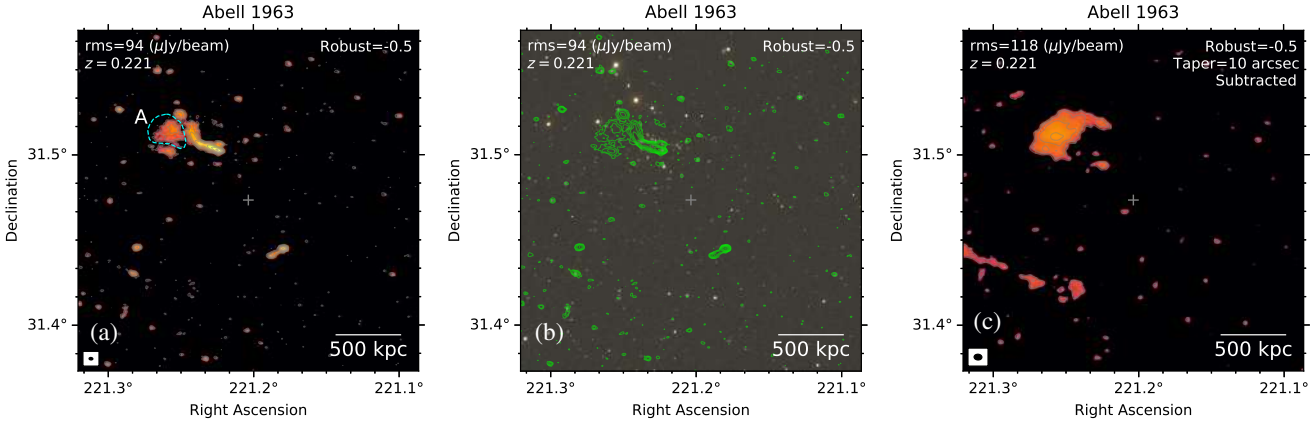

Fig. 8. Abell 1963. Image description is the same as that in Fig. 2.

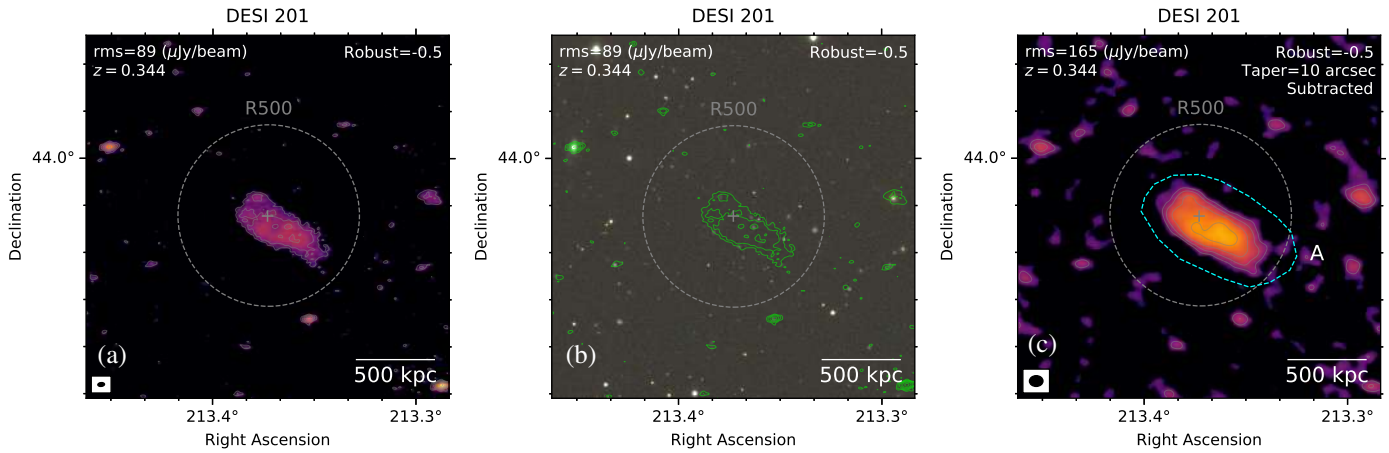

Fig. 9. DESI 201. Image description is the same as that in Fig. 2.

halo emission is patchy in their VLA low-resolution (63″) image and does not follow the ROSAT X-ray emission (see Fig. 1 in Govoni et al. 2012).

LOFAR high-resolution images in Fig. 11 confirm the presence of diffuse emission in MCXC J0928.6+3747. Thanks to the high-resolution images of LOFAR, the diffuse source reported by Govoni et al. (2012) can be resolved into three separated sources, labelled A, B, and C. In the SE direction, 350 kpc from the cluster centre, source A is detected with a projected size of 380 kpc × 250 kpc. The SB of A decreases gradually towards the NW, but its SB rapidly decreases towards the SE. Source B is detected roughly 680 kpc SW from the cluster centre, with a projected size of 260 kpc × 190 kpc. The morphology of B is similar to that of A in which the radial SB gradually increases then sharply decreases in the outer region. Both A and B are not associated with SDSS optical sources (see Fig. 11b). We classify A and B as radio relics. In the discrete-source-subtracted image (the panel c), a low SB emission (C) with a projected size

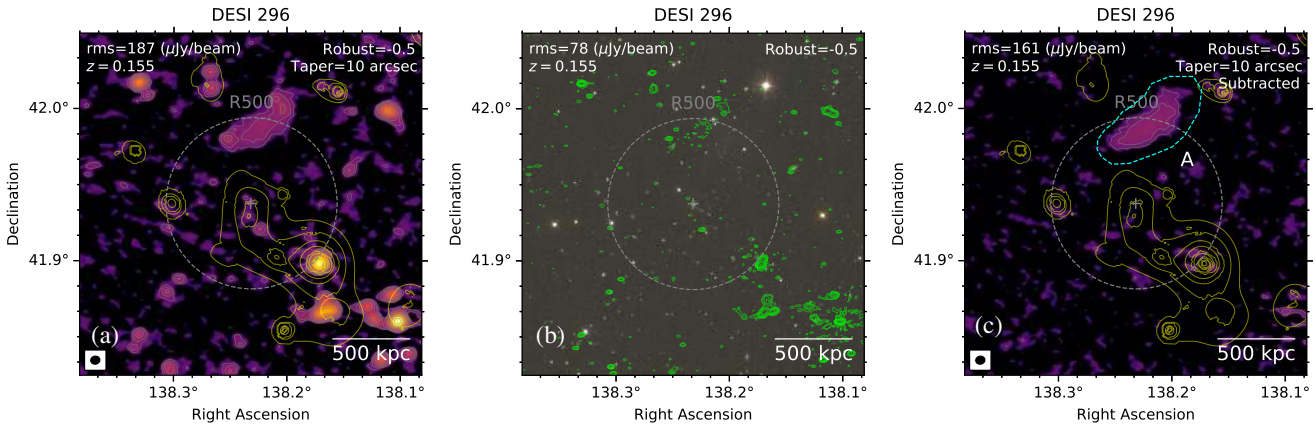

Fig. 10. DESI 296. Image description is the same as that in Fig. 2.

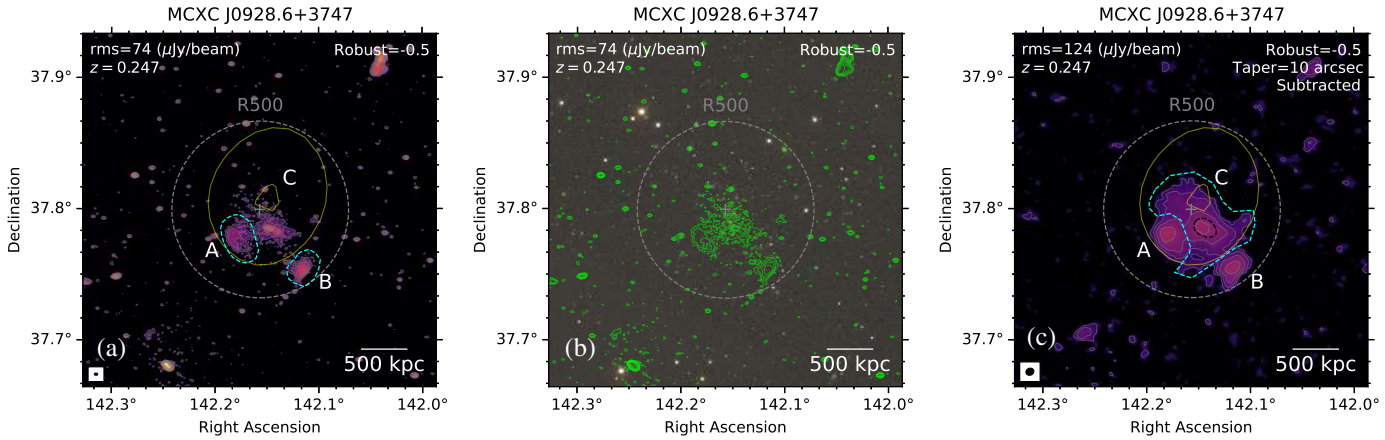

Fig. 11. MCXC J0928.6+3747. Image description is the same as that in Fig. 2.

of 850 kpc × 400 kpc is detected and partly covers the ROSAT X-ray emission in the cluster centre. The extension of source C implies that it is not likely associated with the tailed radio galaxy embedded in the cluster centre. We classify source C as a radio halo, confirming the classification by Govoni et al. (2012).

4.11. MCXC J0943.1+4659

Giovannini et al. (2009) reported the presence of diffuse emission in the central region of MCXC J0943.1+4659 (z = 0.406). The diffuse emission has a size of 400 kpc and is offset from the ROSAT X-ray emission. These authors pointed out that the X-ray emission from the cluster shows double structures that are separated by 2′.

In Fig. 12, the LOFAR images confirm the presence of the diffuse sources in the central region of MCXC J0943.1+4659 and show the new detection of a diffuse source in the NE region of the cluster. The diffuse source, named A, in the NE direction has a projected size of 530 kpc × 460 kpc and is elongated in the N-S direction. The SB of source A increases rapidly from E to W before gradually decreasing towards the W side of the source. In the cluster centre, a diffuse source, named B, is seen in the LOFAR low-resolution images. Source B has a size of 1.2 Mpc in projection. A number of radio galaxies are also seen embedded in the centre of B. The radio emission from source B roughly follows the X-ray emission detected with the *XMM-Newton* observations, unlike what is seen with the VLA 1.4 GHz and ROSAT shallow observations in Giovannini et al. (2009). We classify sources A and B as a radio relic and radio halo, respectively. This is supported by the fact that the X-ray morphology indicates that the cluster is disturbed, as seen in Fig. 12 and Fig. 4 in Giovannini et al. (2009).

4.12. MCXC J1020.5+3922

We discovered a diffuse source, labelled A, towards the SE region of MCXC J1020.5+3922 (z = 0.143), seen in the LOFAR images in Fig. 13. The high-resolution radio emission from source A is patchy. Its projected size is 360 kpc × 230 kpc. The SDSS image in Fig. 13b shows no obvious connection between source A and optical sources in the field. Source A could be an AGN remnant (900 kpc) although further studies are required to confirm its nature.

4.13. MCXC J1711.0+3941

Figure 14 shows that LOFAR observations detect a 600 kpc long narrow-angle tailed (NAT) radio galaxy in MCXC J1711.0+3941 (z = 0.065). The source has an optical counterpart as seen in the SDSS image in panel b of Fig. 14. The tail end of the source is highly extended, 630 kpc × 380 kpc, in the NE-SW direction and is located at the edge of the ROSAT X-ray emission. The formation of the disturbed tail of the radio galaxy remains poorly understood. It might originate from

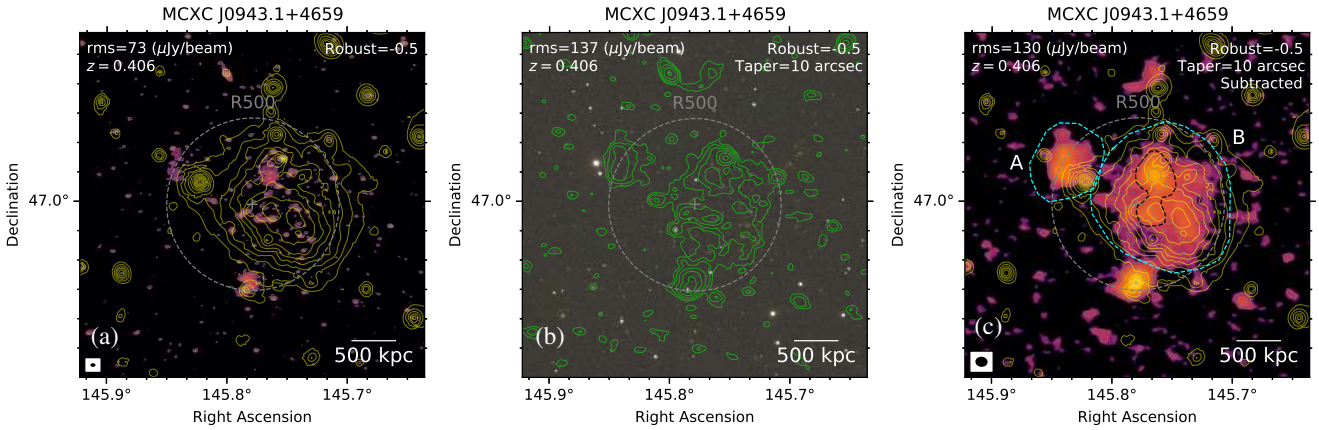

Fig. 12. MCXC J0943.1+4659. Image description is the same as that in Fig. 2.

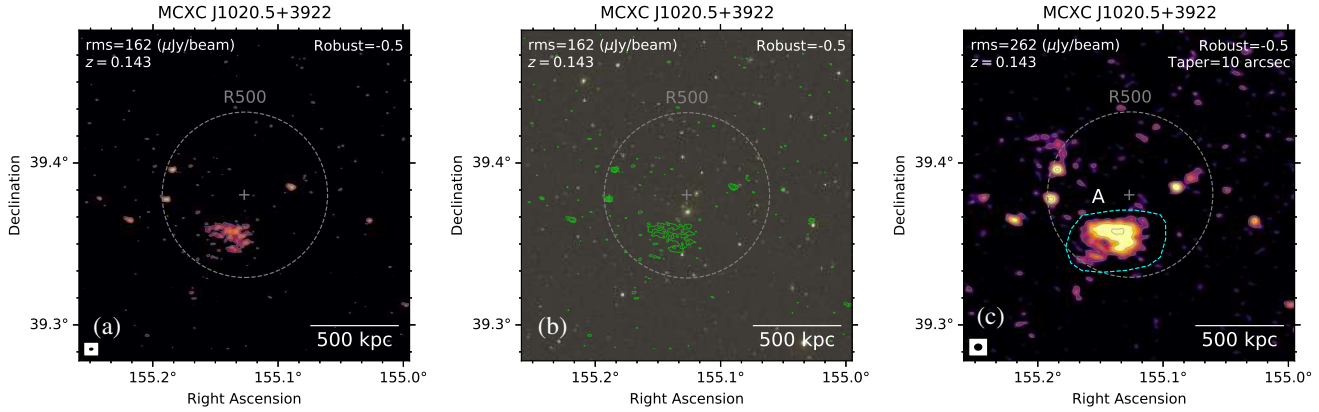

Fig. 13. MCXC J1020.5+3922. Image description is the same as that in Fig. 2.

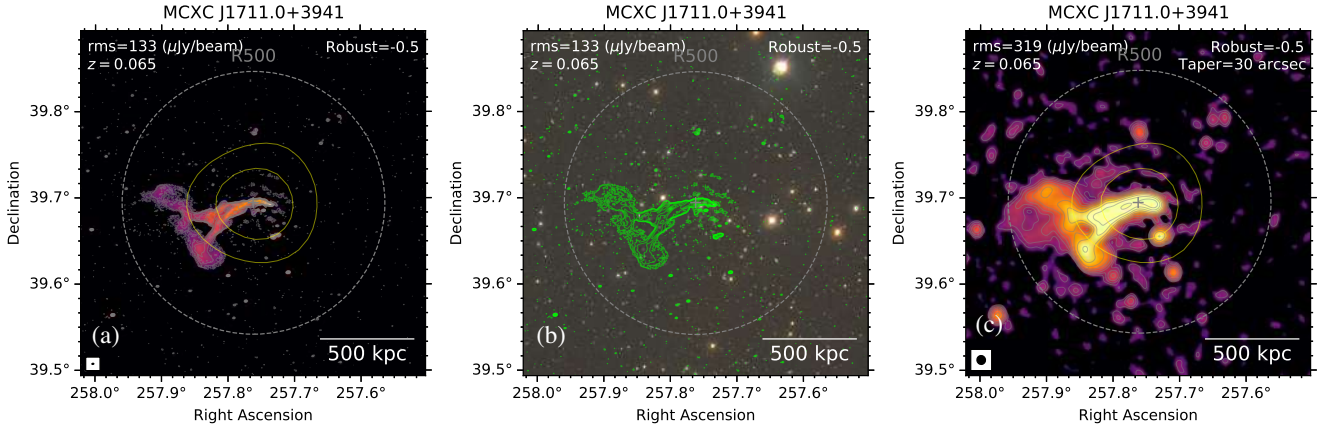

Fig. 14. MCXC J1711.0+3941. Image description is the same as that in Fig. 2.

the interaction between the radio galaxy and the surrounding medium. We do not measure the flux density of the disturbed tail as the boundary between the diffuse emission and the NAT galaxy is unknown.

4.14. PSZRX G095.27+48.27

The LOFAR images in Fig. 15 show the new detection of diffuse sources in the SE and central regions of PSZRX G095.27+48.27 (z = 0.362), labelled A and B. Source A in the SE region has an arc-like shape with a projected size of 1300 kpc × 450 kpc. The width of source A is 90 kpc as measured in the high-resolution image in panel a. The major axis of source A is along the NE-SW direction which is perpendicular to the line connecting the source and the cluster centre. The optical image in panel b shows that source A is not related to any SDSS sources. The location and morphology of source A suggest that it is a radio relic that is generated in a dynamically disturbed cluster with a SE-NW merger axis as confirmed by the SDSS data. In the central region of the cluster, we detect a diffuse source (1200 kpc × 610 kpc) at

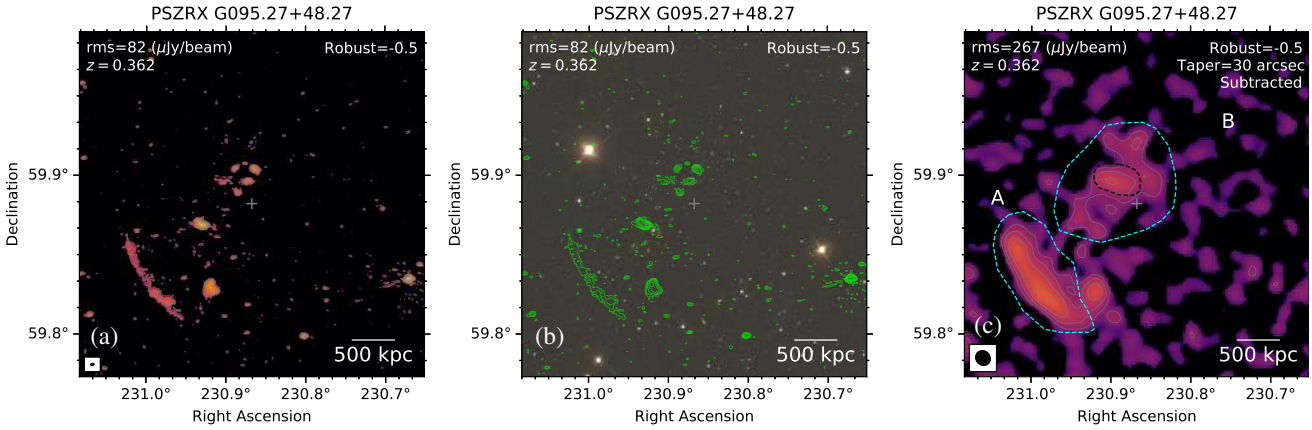

Fig. 15. PSZRX G095.27+48.27. Image description is the same as that in Fig. 2.

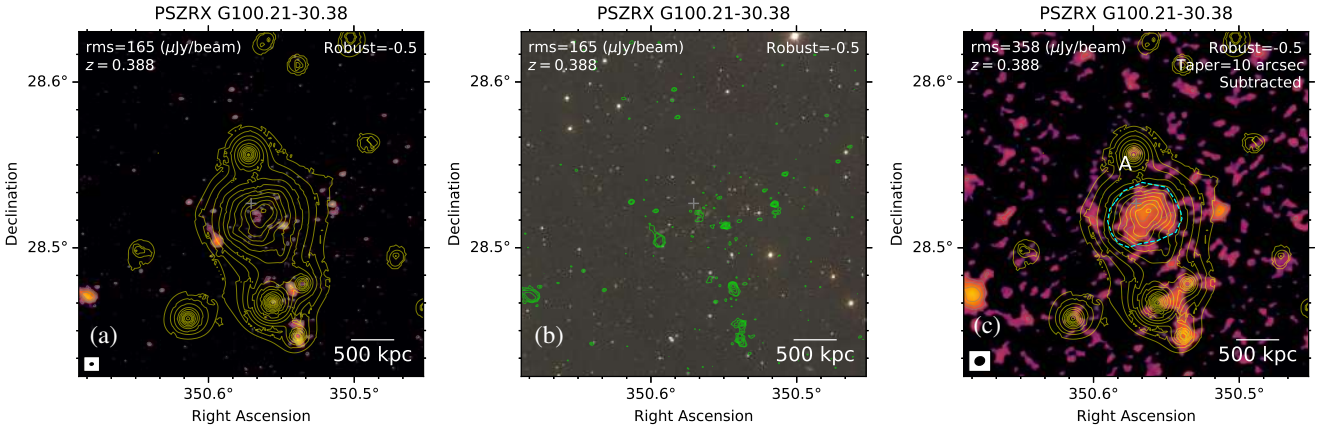

Fig. 16. PSZRX G100.21-30.38. Image description is the same as that in Fig. 2.

2σ that contains a number of radio galaxies and we classify it as a candidate radio halo.

4.15. PSZRX G100.21-30.38

The LOFAR observations shown in Fig. 16 capture a new diffuse radio source in the centre of PSZRX G100.21-30.38 ($z = 0.388$). The diffuse source, named source A, has a size of 600 kpc × 380 kpc and is elongated in the SE-NW direction, which is aligned with the major axis of the galaxy distribution in the cluster, as seen in the SDSS image in panel b. The radio emission from A roughly follows the *XMM-Newton* X-ray emission in the central region which is slightly elongated in the NW-SE direction. The morphology of the X-ray emission indicates that the cluster is in a dynamically disturbed state. We classify source A as a radio halo due to its location, morphology, and its correlation with X-rays.

4.16. PSZRX G102.17+48.88

In Fig. 17 we show LOFAR images of PSZRX G102.17+48.88 ($z = 0.292$). In the low-resolution source-subtracted image (panel a), we detect diffuse emission with a projected size of 460 kpc × 340 kpc, elongated in the north-south direction. To the SE direction, compact radio sources are seen to be associated with SDSS optical counterparts. The galaxy distribution in the optical image is elongated in the NW-SE direction, similar to the orientation of the diffuse radio source. This implies a connection of the diffuse radio source to the morphology of the ICM, suggesting that it could be a radio halo. Although its size is smaller than typically found for radio halos in other systems, this could be due to the lower sensitivity of the observations, which prevents detection of the faint emission in the outer region. Alternatively, the diffuse emission could be related to AGN activities, which could explain the patchy emission in the high-resolution image.

4.17. PSZRX G116.06+80.14

LOFAR observations detect faint diffuse emission, which we name source A, in the central region of PSZRX G116.06+80.14 ($z = 0.518$, the highest-z system in the sample), as seen in Fig. 18. The diffuse source has a projected size of 340 kpc. The high-resolution image shows patchy emission from this source. The radio emission is not spatially correlated with the low-S/N X-ray emission from ROSAT. It is unclear whether source A is part of a larger radio halo or is associated with the compact radio source towards its NE direction.

4.18. PSZRX G181.53+21.43

In Fig. 19, diffuse sources are detected in the outskirts of PSZRX G181.53+21.43 ($z = 0.175$). The diffuse sources are labelled A, B, and C. A new diffuse source (A) with a projected

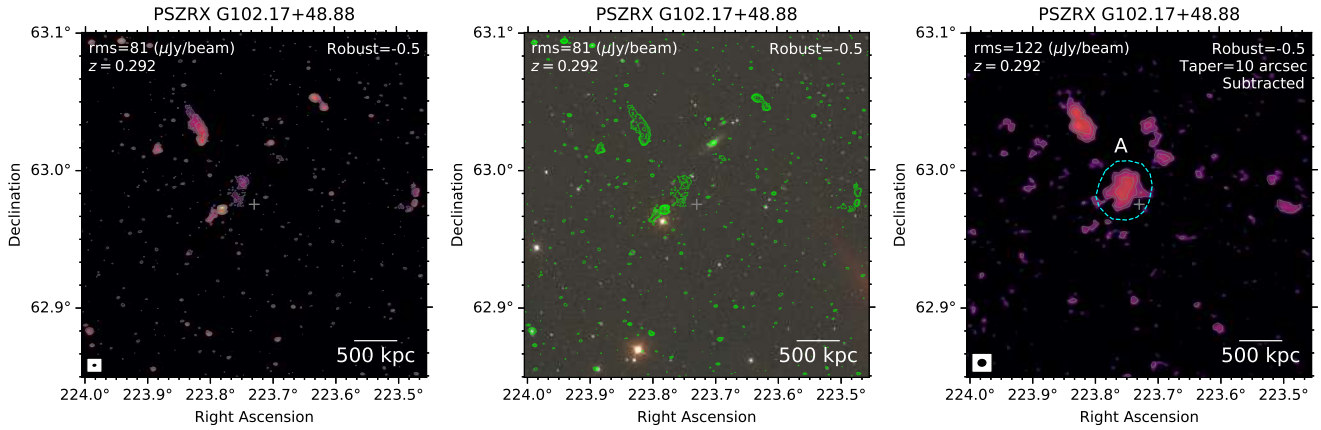

Fig. 17. PSZRX G102.17+48.88. Image description is the same as that in Fig. 2.

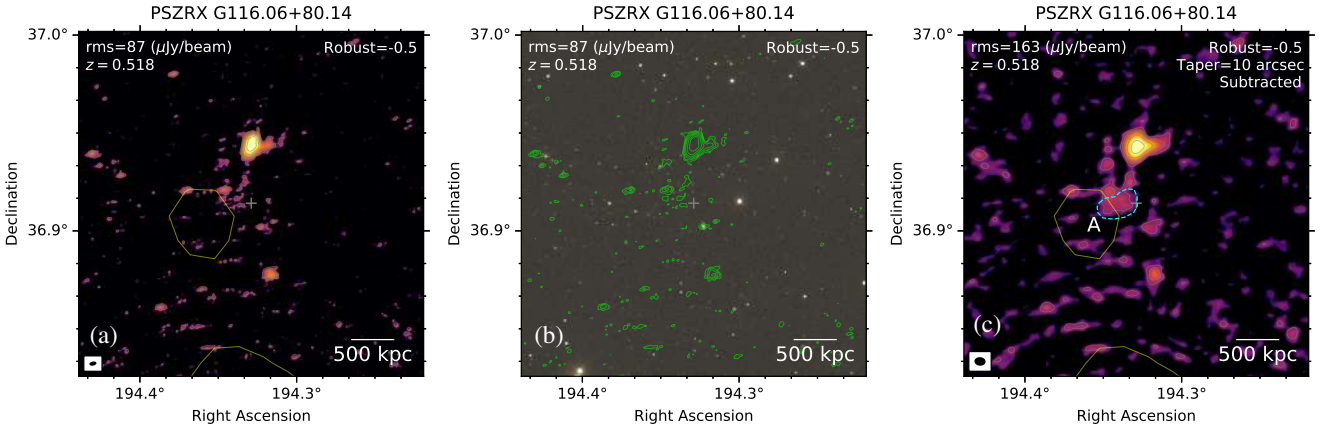

Fig. 18. PSZRX G116.06+80.14. Image description is the same as that in Fig. 2.

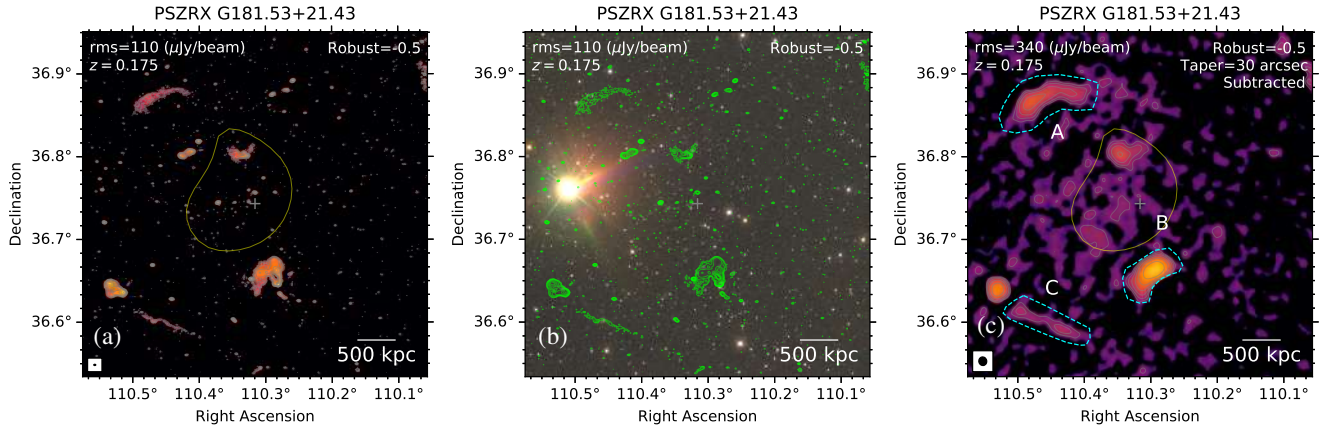

Fig. 19. PSZRX G181.53+21.43. Image description is the same as that in Fig. 2.

size of 1000 kpc × 250 kpc elongated in the NW-SE direction is detected 1.7 Mpc northeast of the cluster centre. Source A is not obviously connected to any SDSS optical sources, as seen in panel b of Fig. 19. The observed properties of source A suggest that it is a radio relic. We find a wide-angle tailed (WAT) radio galaxy 1 Mpc SW of the cluster centre with its core in the outer region. The end tail of the WAT radio galaxy (source B) is highly disturbed and is oriented in a direction similar to the major axis of source A. The optical SDSS image shows that most of the galaxies are distributed in the NE-SW direction, implying that A and B have been shaped by the dynamics of the cluster. In the SE region, a thread-like source (C; 900 kpc × 90 kpc in projection) is seen in the LOFAR images. An SDSS optical counterpart in the middle of C suggests that it is a Fanaroff-Riley class I (FR-I) radio galaxy. In the central region of the cluster, there is a hint of diffuse emission which might be a tentative faint radio halo. We do not measure the size or the flux density of the candidate halo as its boundary is unclear in the current images.

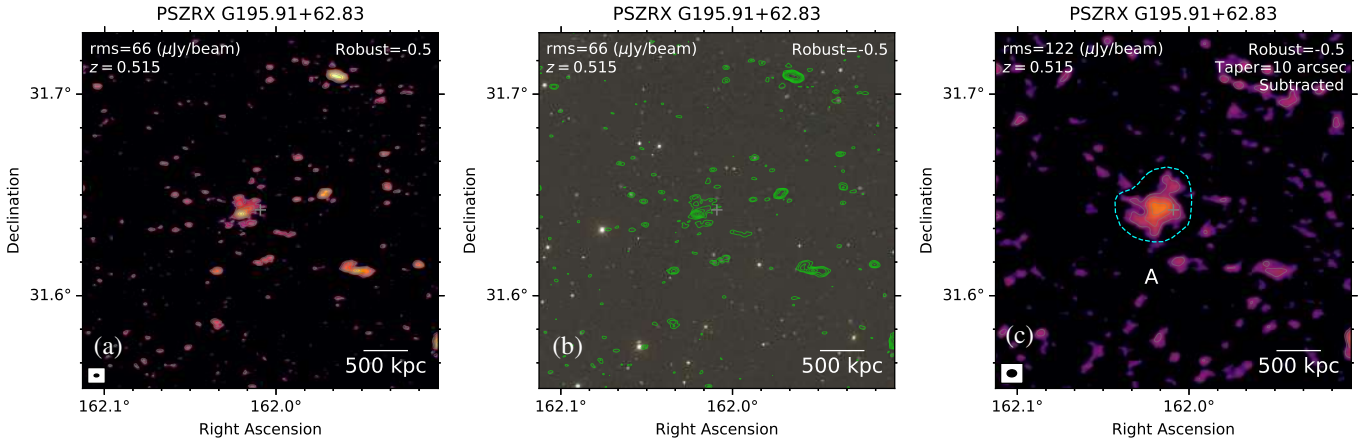

Fig. 20. PSZRX G195.91+62.83. Image description is the same as that in Fig. 2.

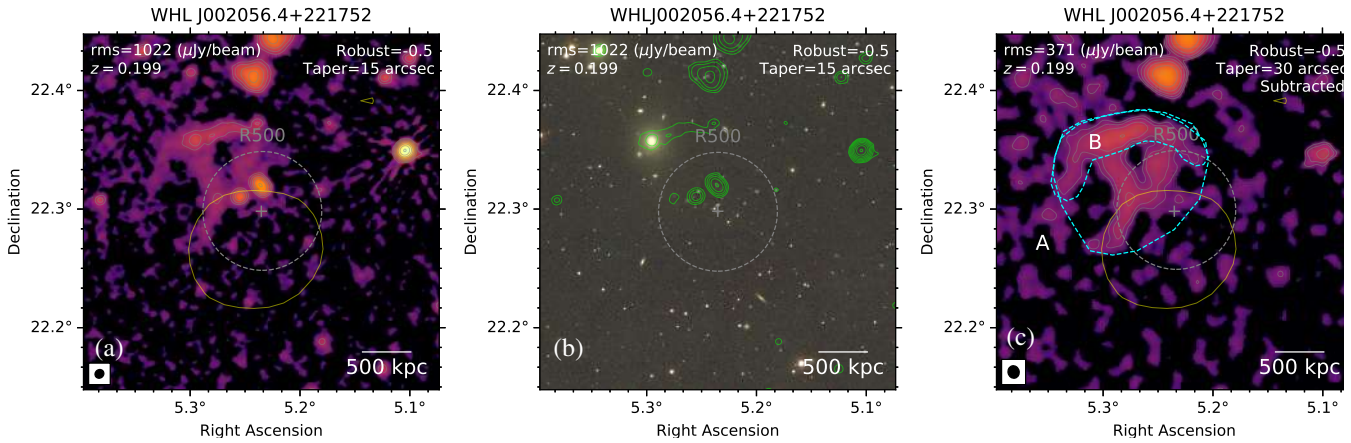

Fig. 21. WHL J002056.4+221752. Image description is the same as that in Fig. 2.

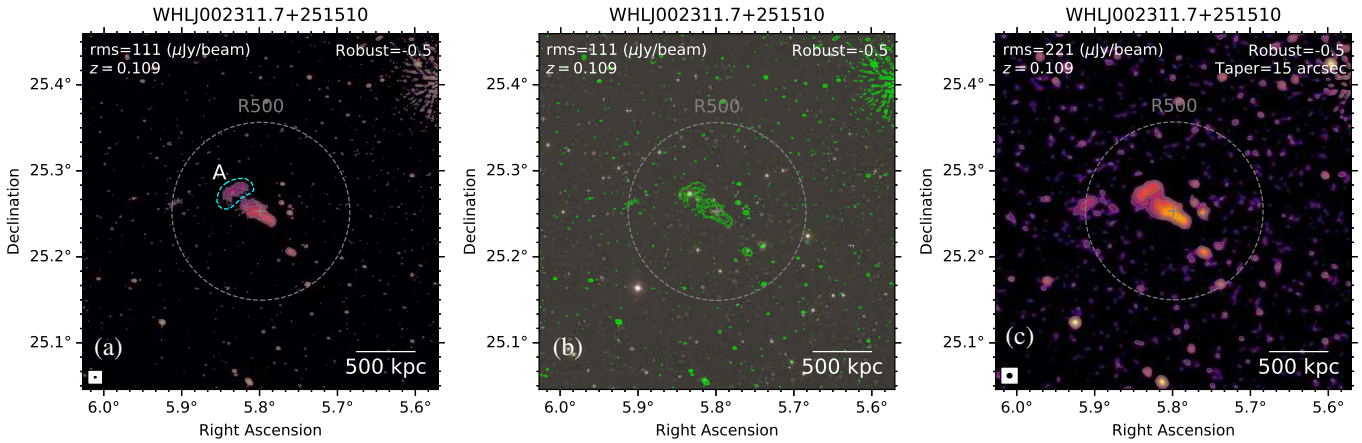

Fig. 22. WHL J002311.7+251510. Image description is the same as that in Fig. 2.

4.19. PSZRX G195.91+62.83

In Fig. 20, LOFAR images show the presence of a new diffuse radio source around a radio galaxy in the centre of PSZRX G195.91+62.83 (z = 0.515). When removing the emission from the radio galaxy, a diffuse source is seen in the low-resolution image (shown in panel c). The diffuse source has a projected size of 600 kpc and we classify it as a radio halo.

4.20. WHL J002056.4+221752

As seen in the LOFAR images in Fig. 21, a new diffuse structure is seen in the NE region of the galaxy cluster WHL J002056.4+221752 (z = 0.199). The entire diffuse structure, labelled A, has a rectangular shape, spanning from the cluster centre to 750 kpc in the outskirts. The outer size of the source (1 Mpc) is smaller than that of the inner region (640 kpc). The source, named source B, is brightest in the northern region. In

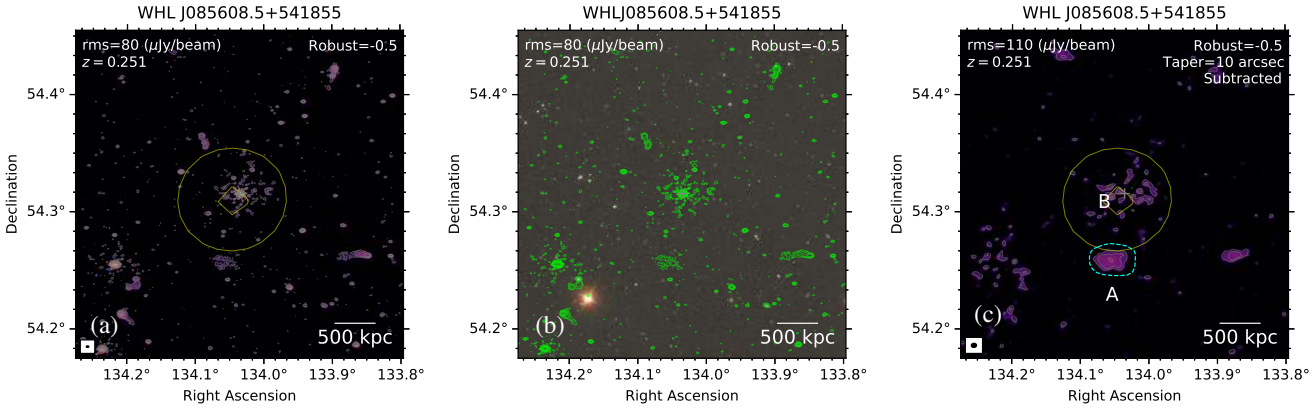

Fig. 23. WHL J085608.5+541855. Image description is the same as that in Fig. 2.

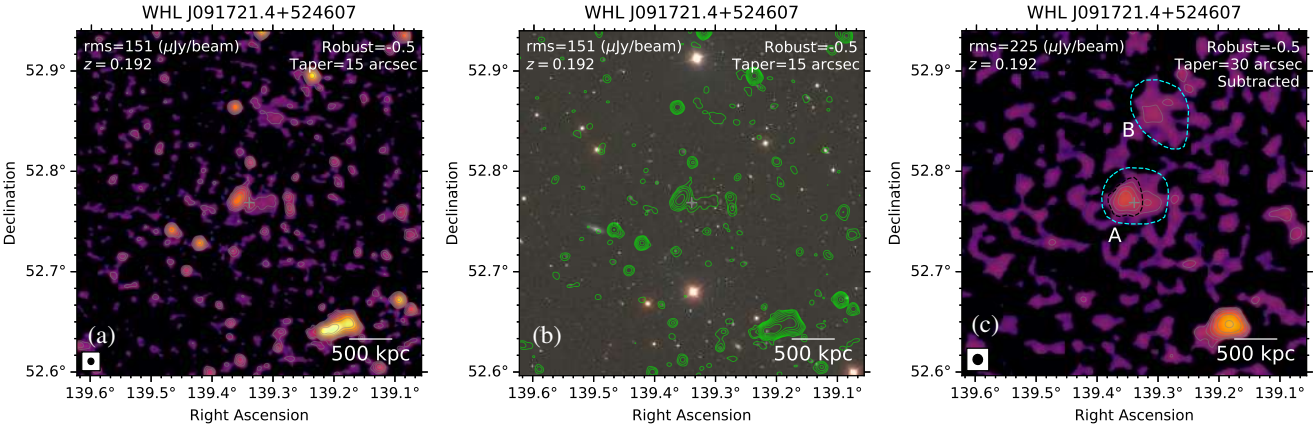

Fig. 24. WHL J091721.4+524607. Image description is the same as that in Fig. 2.

the panels b and c, two compact radio galaxies are found on the southern side of the structure. It is unclear whether or not the radio galaxies physically connect to the northern structure. The nature of the radio diffuse structure is unknown.

4.21. WHL J002311.7+251510

In Fig. 22, a tailed radio galaxy is detected with LOFAR in the centre of the galaxy cluster WHL J002311.7+251510 (z = 0.109). Excess diffuse emission with a projected size of 230 kpc × 120 kpc is detected at the end of the tail. In the high-resolution image, the diffuse source is detached from the tailed galaxy and does not have an SDSS optical counterpart. However, we cannot exclude that it is related to the radio galaxy. The flux density of the diffuse source at 144 MHz is 47.9 ± 4.9 mJy but its nature remains unknown.

4.22. WHL J085608.5+541855

LOFAR images of WHL J085608.5+541855 (z = 0.251) are shown in Fig. 23. The cluster hosts a newly detected 380 kpc × 210 kpc diffuse source in the southern region, 900 kpc from the cluster centre. The diffuse source is patchy at high resolution and is not clearly associated with any SDSS sources. The source could be a remnant from AGN activity. We measure the flux density and radio power of the diffuse source and present the measurements in Table 2. In the cluster central region, multiple small-scale radio sources are detected around the central radio galaxy. These sources are likely artefacts around the radio galaxy in the cluster centre.

4.23. WHL J091721.4+524607

LOFAR images uncover the presence of multiple radio sources in the galaxy cluster WHL J091721.4+524607 (z = 0.192) seen in Fig. 24. The diffuse emission in the cluster centre, labelled A, has a projected size of 290 kpc × 170 kpc, and is oriented in the E-W direction. It is unclear whether A is connected to a radio galaxy 270 kpc to the east or they are seen in projection. Due to its small detected size and the possible connection with a radio galaxy, the classification of source A is difficult. A diffuse source, named source B, is seen in the low-resolution image in panel c of Fig. 24, 1 Mpc to the north of the cluster centre. Source B with a projected size of 500 kpc × 300 kpc is detected at 2σ. The morphology of source B at high resolution (panel a) implies that it may connect to an FR-I galaxy, which does not have an SDSS optical counterpart.

4.24. WHL J101350.8+344251

In Fig. 25, LOFAR images of WHL J101350.8+344251 (z = 0.146) show the new detection of multiple diffuse sources, labelled A, B, and C. A diffuse source (A) with a projected size of 310 kpc × 150 kpc is detected about 540 kpc from the cluster centre towards the SE. The major axis of the source is perpendicular to the axis connecting the cluster centre and the source.

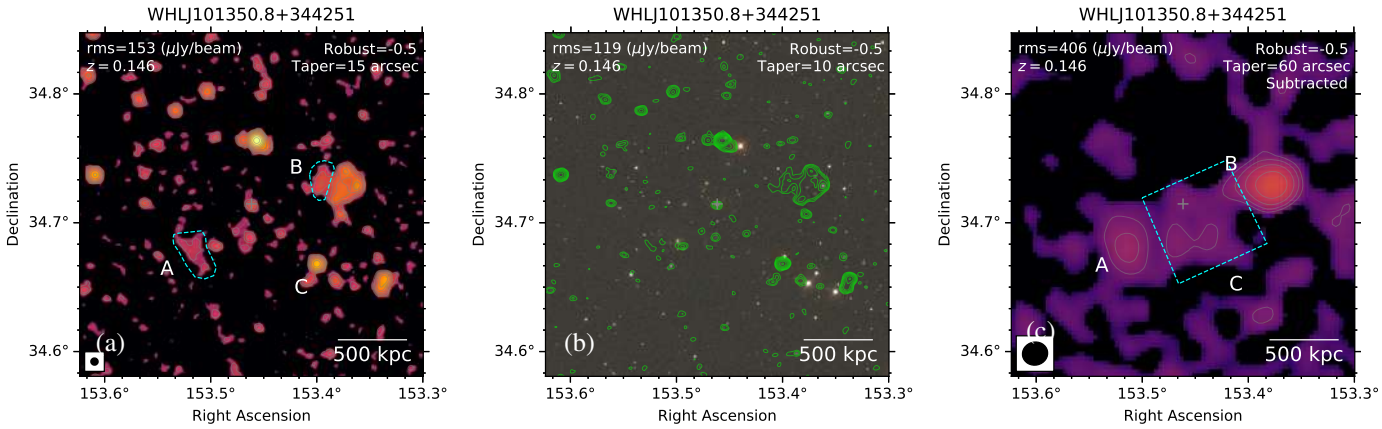

Fig. 25. WHL J101350.8+344251. Image description is the same as that in Fig. 2.

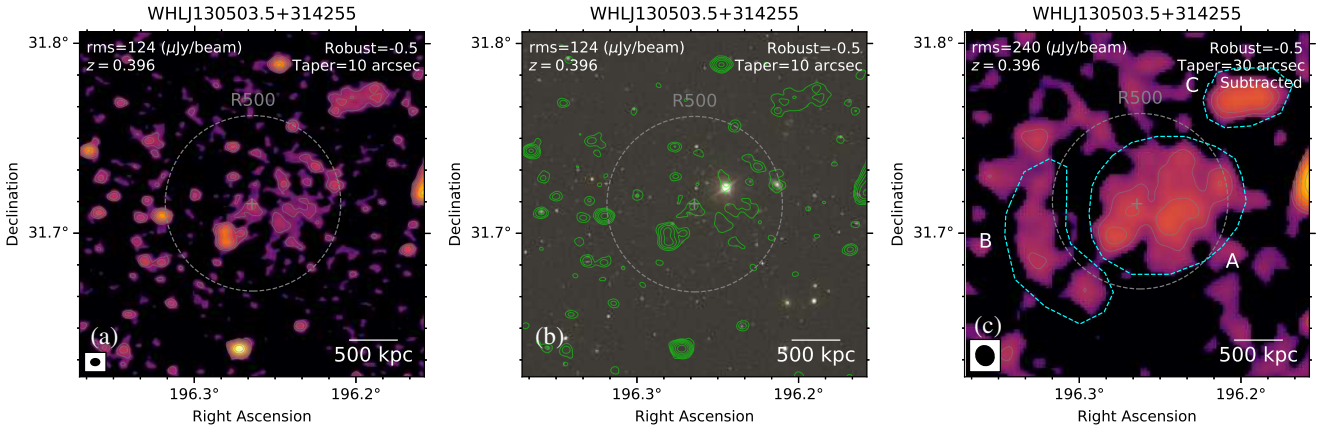

Fig. 26. WHL J130503.5+314255. Image description is the same as that in Fig. 2.

There is no optical counterpart to A in the SDSS data and we classify it as a radio relic. To the west of the cluster, a WAT radio galaxy is detected that has an SDSS optical counterpart in the central bright part. Interestingly, excess diffuse emission (B) is seen in the eastern region behind the tailed galaxy. The nature of B is still unknown. In the central region of the cluster, faint emission (C) is detected at 2σ connecting A and B that spans a projected area of 900 kpc × 300 kpc. We classify C as a candidate radio halo. The flux density and radio power of the sources are given in Table 2.

4.25. WHL J130503.5+314255

Three new diffuse sources are detected with LOFAR in WHL J130503.5+314255 (z = 0.396), labelled A, B, and C in Fig. 26. In the cluster centre, a faint diffuse source (A) is detected at $>2\sigma$ and has a projected size of 1400 kpc × 800 kpc, oriented in the EW direction. Multiple radio sources from individual galaxies are embedded in the region of source A. As source A is unlikely to be a combination of these discrete sources, we classify it as a radio halo. In the eastern direction, an arc-like diffuse (1400 kpc × 320 kpc) source is also detected at 2σ which we classify as a candidate radio relic. In the NW region (1.3 Mpc), we detect a diffuse (720 kpc × 360 kpc) source (C) that has no clear counterpart in the SDSS image. The major axis of source B is oriented E to W. It is unclear how source B is formed.

4.26. WHL J165540.4+334422

Figure 27 shows the new detection of a diffuse source in the western region of WHL J165540.4+334422 (z = 0.255). Its projected size is 630 kpc × 400 kpc. The projected distance from the diffuse source to the reported cluster centre from the Wen & Han (2015) catalogue is 2′ (480 kpc). We classify the diffuse source as fossil plasma originating from radio galaxies.

4.27. WHL J172125.4+294144

As seen in Fig. 28, LOFAR observations of WHL J172125.4+294144 (z = 0.184) detect two diffuse sources, labelled A and B, in the western region of the cluster and separated by a distance of 1.3 Mpc and 2.2 Mpc, respectively, from the cluster centre. The sizes of these sources are 560 kpc × 260 kpc and 600 kpc × 340 kpc. There is an optical source near the peak of the northern part of source A, but the optical source is not likely to generate the large structure of source A. It is unclear how source A is formed but they could be related to fossil plasma from AGN activities. The surface brightness of source B decreases sharply in the outside region which is consistent with it being a relic. No diffuse emission is seen in the central region of the cluster with the LOFAR observations.

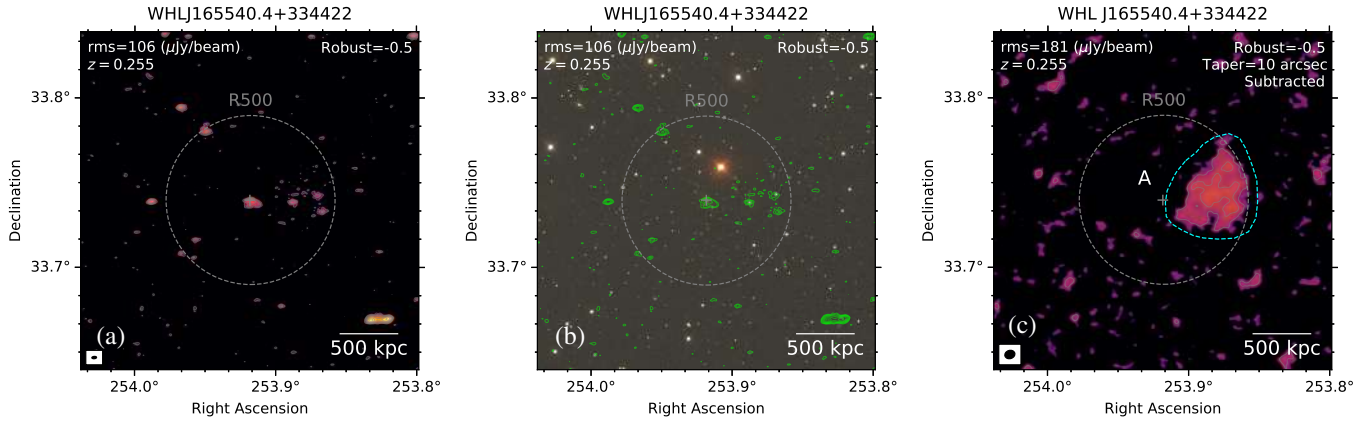

Fig. 27. WHL J165540.4+334422. Image description is the same as that in Fig. 2.

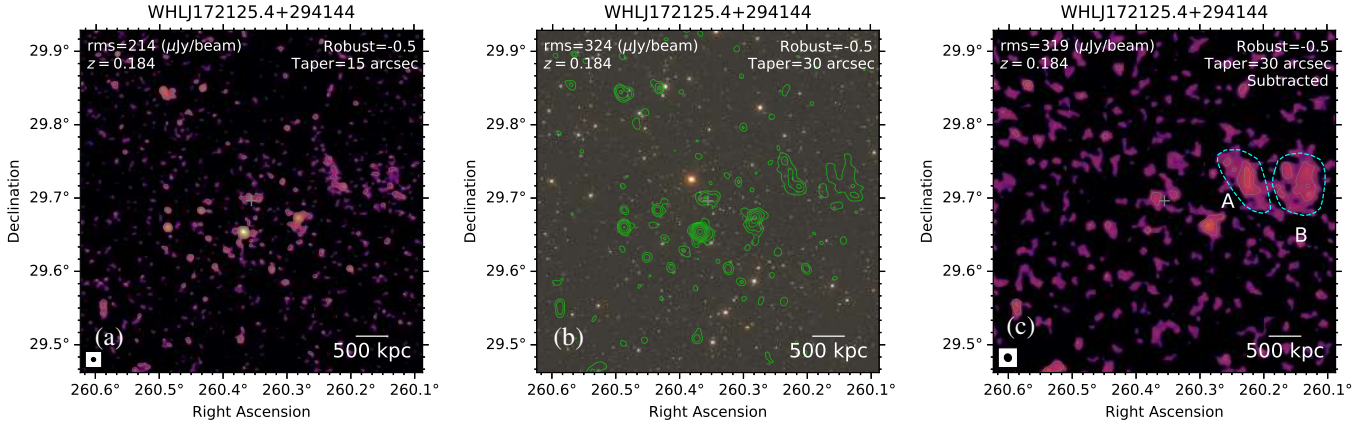

Fig. 28. WHL J172125.4+294144. Image description is the same as that in Fig. 2.

4.28. WHL J173424.0+332526

In Fig. 29, LOFAR observations show diffuse sources in the northern region of the galaxy cluster WHL J173424.0+332526 (z = 0.485). The diffuse source, labelled A, might be associated with an SDSS optical galaxy to the north. The southern side of A is more extended towards the centre of the cluster. Further to the north, there is a cap-shaped source (named B). It is unclear whether these diffuse sources are connected and their origin is unknown.

5. Discussion

5.1. Source classification

Diffuse radio sources, particularly halos and relics, are not well studied in low-mass ($M_{500} \lesssim 4 \times 10^{14}\,M_{\odot}$) clusters. One reason is related to their expected lower luminosity, which runs into the sensitivity limits of current instruments. The other reason is linked to the steep-spectrum ($\alpha < -1$) nature of diffuse sources, which makes them difficult to detect at high frequencies (above ~1 GHz). These limitations imply that diffuse sources may be best detected with deep observations at low radio frequencies such as those between 120 MHz and 168 MHz provided by LoTSS-DR2. Diffuse radio sources associated with disturbed clusters that are less massive than $4 \times 10^{14}\,M_{\odot}$ have only been found in a handful of cases. For radio halos, these systems include Abell 3562 (Venturi et al. 2003; Giacintucci et al. 2005); Abell 2061 (Rudnick & Lemmerman 2009); PSZ1 G018.75+23.57 (Bernardi et al. 2016); Abell 2146 (Hlavacek-Larrondo et al. 2018; Hoang et al. 2019); RXC J1825.3+3026 (Botteon et al. 2019); Abell 1775 Botteon et al. (2021b), Ant cluster (Botteon et al. 2021a), Abell 990 (Hoang et al. 2021), MCXC J1036.1+5713 (Osinga et al. 2021), PSZ2 G040.58+77.12, PSZ2 G031.93+78.71, PSZ2 G112.48+56.99, PSZ2 G189.31+59.24, PSZ2 G048.10+57.16, PSZ2 G192.18+56.12, PSZ2 G049.32+44.37, PSZ2 G179.09+60.12, and PSZ2 G172.63+35.15 (Botteon et al. 2022). For relics, the low-mass systems hosting relic(s) that have been reported in the literature are ZwCl 0008.8+5215 (Feretti et al. 2012; van Weeren et al. 2011), Abell 1240 (Kempner & Sarazin 2001; Bonafede et al. 2009; Hoang et al. 2018), Abell 3376 (Bagchi et al. 2006), PSZ1 G096.89+24.17 (De Gasperin et al. 2014; Jones et al. 2021), Abell 168 (Dwarakanath et al. 2018), Abell 1904 van Weeren et al. 2021), PSZ2 G080.16+57.65, PSZ2 G099.48+55.60, PSZ2 G048.10+57.16, PSZ2 G165.46+66.15, and PSZ2 G057.61+34.93 (Botteon et al. 2022).

In this paper, we report the discovery of diffuse radio sources in 28 non-PSZ2 galaxy clusters in the LoTSS-DR2 fields. More specifically, radio halos are detected at high confidence in six clusters and there are a further seven tentative detections of halos. Eleven clusters host one or more radio relics (11 confirmed and three candidate relics). Among these clusters hosting relics, three systems have two relics either on opposite sides of the cluster centre or at 90-degree angles. Seven clusters host both a confirmed or candidate radio halo and radio relics. Five diffuse radio sources in the cluster sample are connected to

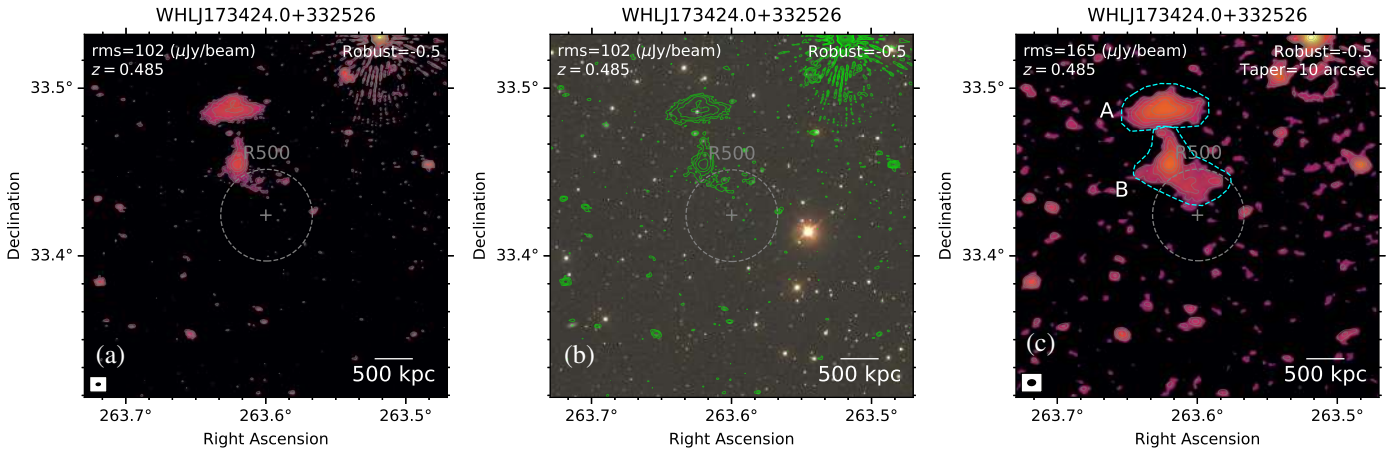

Fig. 29. WHL J173424.0+332526. Image description is the same as that in Fig. 2.

tailed radio galaxies. Thirteen diffuse sources in 11 clusters are unclassified.

The galaxy clusters in our sample are mostly low-mass ($M_{500} \lesssim 4 \times 10^{14}\,M_{\odot}$) systems, except for PSZRX G100.21-30.38 ($M_{500} = 5.71 \times 10^{14}\,M_{\odot}$), PSZRX G116.06+80.14 ($M_{500} = 6.74 \times 10^{14}\,M_{\odot}$), and PSZRX G195.91+62.83 ($M_{500} = 5.55 \times 10^{14}\,M_{\odot}$). Furthermore, 11 of the 13 halos or tentative halos described here are new detections. Whilst we have attempted to carefully classify the sources mainly based on their morphology and location obtained from the LOFAR maps, many sources (13) remain unclassified for a number of reasons. Firstly, the lack of X-ray data prevents us from comparing thermal to non-thermal emission. For instance, the radio emission from halos is known to correlate with the thermal X-ray emission of the ICM. However, X-ray archival data are only available for 13 clusters, 9 of which have data from low-resolution, shallow observations with ROSAT (see Table 1). The lack of X-ray emission from the other clusters (i.e. Abell 1330, PSZRX G095.27+48.27, WHL J101350.8+344251, and WHL J165540.4+334422) that potentially host a radio halo prevents us from firmly classifying the diffuse sources. Similarly, the relative location of elongated relics with respect to the thermal ICM, which could help in the classification of such sources, is unknown. Furthermore, sensitive X-ray data are missing for several candidate relics (i.e. Abell 1943, Abell 1963, WHL J130503.5+314255, WHL J173424.0+332526). Secondly, ancillary radio data at different frequencies that might provide crucial information on the spectral and polarimetric properties of the diffuse sources are largely unavailable. Thirdly, the observed sizes of the diffuse radio sources of some of our low-mass clusters are not as large as those in massive systems and make the distinction between diffuse sources and radio galaxies more difficult. Therefore, to understand the nature of the diffuse sources, multi-wavelength X-ray and high-frequency polarimetric radio observations are needed. In addition, deeper low-frequency radio observations might also help with the classification of diffuse sources of small angular sizes.

Finally, we note that our visual classification (VC) of diffuse radio sources has been a conscientious procedure and even then there is some ambiguity regarding classifications. Alternative approaches such as by Botteon et al. (2022) make use of a decision tree classification (DTC) to render classifications more reproducible. We apply the DTC to classify the diffuse sources in our sample. The resulting classification is given in Table 2 (i.e. Col. 4). In general, our VC is roughly in agreement with the results from DTC, especially for halos and relics. The sources are classified as no diffuse emission (NDE) by DTC if they are clearly associated with AGN or unclassified (U) in some cases in our VC. For instance, source C in PSZRX G181.53+21.43 is classified as an AGN in our VC, but is listed as NDE by DTC; source A in Abell 1213 is unclassified (U) by VC, but is NDE in the DTC. Nevertheless, from the many different morphologies, brightnesses, and levels of contamination, our study highlights that classification will remain a challenge with deep, low-frequency surveys where our target sources are often embedded in a sea of abundant low-energy electrons that are particularly abundant at low frequencies. Techniques based on machine learning may be promising but even then it is apparent that robust classifications are a formidable challenge (see e.g., Aniyan & Thorat 2017; Lukic et al. 2019; Vavilova et al. 2021).

Table 3. Best-fit parameters for cluster mass calibration.

Catalogues	a	b	R^2
PSZ2 – DESI	0.95 ± 0.01	0.02	0.92
PSZ2 – MCXC	0.85 ± 0.02	0.17 ± 0.02	0.68
PSZ2 – comPRASS	0.96 ± 0.02	0.04 ± 0.02	0.56
PSZ2 – WHL	0.87 ± 0.05	0.04 ± 0.04	0.46

5.2. Cluster-mass calibration

The masses of the galaxy clusters in the sample are shown in Table 1 (Col. 7). For the DESI, MCXC, and comPRASS clusters, we use the estimates reported in the corresponding catalogues. The masses of the WHL clusters presented in Table 1 are not available, but they have richness estimates. This allows us to obtain the M_{500} of the WHL clusters using the M_{500}–richness scaling relation in Eq. 17 of Wen & Han (2015).

We note that there may also be unknown systematic uncertainties associated with the masses for the clusters in our sample, because they are estimated with different methods using multi-wavelength data sets. We therefore search for such offsets and re-calibrate the mass estimates against the PSZ2 catalogues to make them consistent. To do this, we first cross-match the PSZ2-detected clusters with those in the DESI, MCXC,

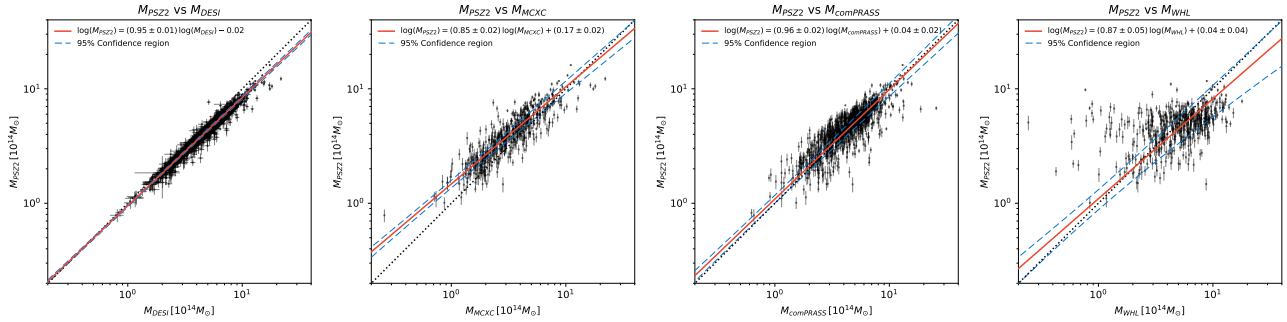

Fig. 30. Scatter plots for the cluster mass reported in the PSZ2 catalogue and that reported in the DESI, MCXC, comPRASS, and WHL catalogues (*from left to right*). The red line indicates the best-fit correlation obtained by the orthogonal distance regression. The dashed blue lines show the 95% confidence region. The dotted black line shows the diagonal line.

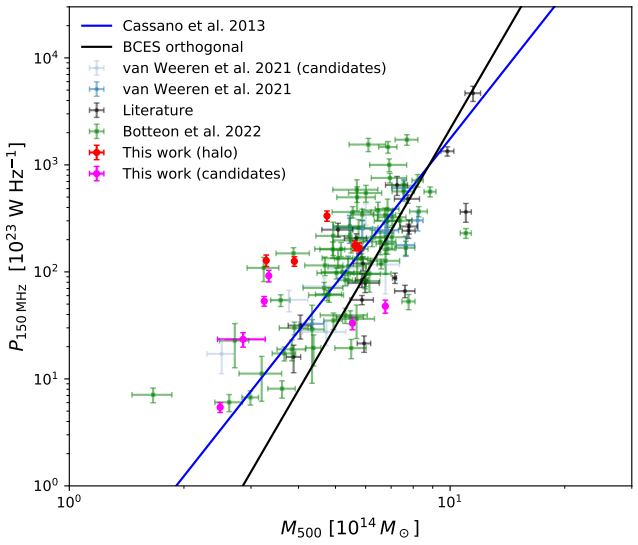

Fig. 31. 150 MHz radio power versus (scaled) mass plot for radio halos. To be consistent with the estimates reported in literature, the halo radio power in our sample is scaled to 150 MHz, assuming a spectral index of −1.2. The plot is adapted from van Weeren et al. (2021).

comPRASS, and WHL catalogues within 5′ (i.e. roughly equal to the resolution of the PSZ2 survey) using `TOPCAT` (Taylor 2005). In the case where a PSZ2 cluster is matched with multiple clusters in the other catalogues, the closest pair with smallest angular separation is chosen. In addition, we select only the pairs that have mass reported in both cross-matched catalogues. With these selection criteria, we find that the numbers of PSZ2 clusters in common with these catalogues are 1094, 527, 939, and 460, respectively. Using the `Scipy` package[7], we perform an orthogonal distance regression (Brown & Fuller 1990) to the cluster masses that are in both PSZ2 and one of the other catalogues:

$$\log M_{\rm PSZ2} = a \log M_{\rm x} + b, \tag{4}$$

where $M_{\rm PSZ2}$ is the M_{500} mass for the clusters in the PSZ2 catalogue; $M_{\rm x}$ is the M_{500} mass for the DESI, MCXC, comPRASS, or WHL clusters; and a and b are free parameters. We make use of all common clusters in the cross-matched catalogues to estimate the best-fit parameters, which are summarised in Table 3. The best-fit correlations are presented in Fig. 30. The mass for the clusters in the DESI, MCXC, and comPRASS catalogues is well correlated with that reported in the PSZ2 catalogue. For the WHL clusters, their mass does not tightly follow that of the PSZ2 clusters, especially in the low-mass regime ($M_{500} < 2{\times}10^{14}M_\odot$).

We now use the best-fit relation in Eq. (4) to re-scale the mass of the galaxy clusters in our sample to that in the PSZ2 catalogue and calculate the scaled mass ($M_{500}^{\rm scaled}$) for these clusters. The resulting scaled mass is listed in Table 1 (Col. 8). In the following analysis, we use the scaled mass instead of the original estimates reported in the DESI, MCXC, and comPRASS catalogues and the WHL mass calculated from the M_{500}–richness relation.

The galaxy clusters from the optical Abell catalogues do not have mass estimates. We find that five Abell clusters in the sample are reported in the WHL catalogue. Two of them have mass estimates, namely Abell 84 and Abell 1889 with cluster sequence numbers (Seq) of 52 and 893, respectively. For the other Abell clusters (i.e. Abell 1330, Abell 1943, and Abell 1963), a mass estimate is not available. We follow the procedure for the WHL clusters described above to calculate the scaled mass ($M_{500}^{\rm scaled}$) of these Abell clusters (see Table 1, Col. 8).

5.3. Scaling of luminosity of diffuse sources with cluster masses

In Fig. 31, we show the scaling of the radio power versus cluster masses for radio halos, adapting the plot from van Weeren et al. (2021). The radio power for the halos in our sample is scaled to that at 150 MHz, using the 144 MHz estimates in Table 2 and assuming an index of −1.2 for the radio power spectrum. Abell 373 does not have a mass estimate and the power for the tentative halo in PSZRX G181.53+21.43 is not measured because of the low-S/N detection. These two clusters are not shown in the plot. We also include the measurements for the PSZ2 clusters from Botteon et al. (2022) who present 12 halos in common with van Weeren et al. (2021). We display only the values for these common clusters reported in Botteon et al. (2022). In Fig. 31, the black line shows the bivariate correlated errors and intrinsic scatter (BCES) orthogonal fit in van Weeren et al. (2021) with a slope of 6.13 and the blue line is the result from Cassano et al. (2013) with a slope of 4.51. The confirmed halos from this paper are shown in red and the tentative halos are in magenta. As expected, the halos from our sample lie at lower masses than the halos that were taken from the literature. The radio powers of the halos lie above the correlation with two exceptions (i.e. the candidate halos in Abell 1330 and PSZRX G116.06+80.14). However, as our sample does not obey any clearly defined selection criteria, it

[7] https://scipy.org

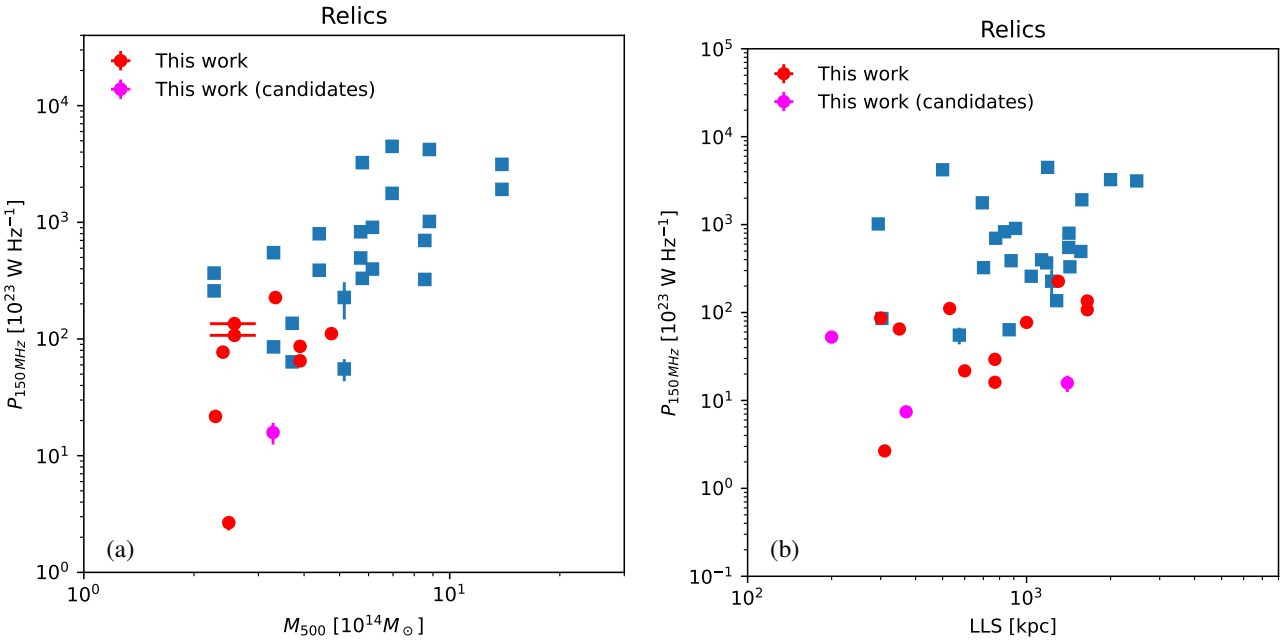

Fig. 32. Radio power, $P_{150\,\mathrm{MHz}}$, vs. scaled mass (*a*) and $P_{150\,\mathrm{MHz}}$ vs. LSS (*b*) for radio relics. Data for other clusters are taken from De Gasperin et al. (2014).

suffers from a bias as the more luminous halos are easier to find. A carefully defined cluster sample at low masses is required in order to study the occurrence at lower masses and to determine whether or not the correlation is flatter at lower masses.

The total energy released in a merger between two clusters of mass M is given by $E \propto M^2/R_{\mathrm{vir}}$, where $R_{\mathrm{vir}} \propto M^{1/3}$. Assuming that the radio luminosity scales as $P \propto E/t_{\mathrm{h}}$, where t_{h} is the life time of the radio halo, we would obtain $P \propto M^{5/3}$ if t_{h} were independent of the cluster mass. If the luminosity–mass correlation is steeper than 5/3, this would imply that halos in higher mass clusters have a shorter lifetime. Our new data suggest that the correlation may not be as steep as the fit from van Weeren et al. (2021). In favour of this picture, the measurements for the halos in the PSZ2 clusters by Botteon et al. (2022) (i.e. the green data points in Fig. 31) indicate a flatter slope. A detail study of the $P - M$ correlation is being carried out by Cuciti et al. (in prep.).

In Fig. 32 we plot the radio power, $P_{150\,\mathrm{MHz}}$, versus mass and $P_{150\,\mathrm{MHz}}$ versus largest linear size (LSS) for radio relics. Data for other clusters are taken from De Gasperin et al. (2014) and are scaled to 150 MHz using the spectral indices therein. For the relics without a spectral index estimate, we assume a value of −1.2. The radio power of relics in lower-mass clusters appears to follow the trend of the higher mass clusters, namely that clusters of greater mass host more powerful radio relics. However, similarly to the relics in higher mass clusters, the LLSs of relics in the low-mass clusters do not appear to show any significant trends. The scaling relations for a larger sample of relics in the LoTSS-DR2 fields are studied in more detail in Jones et al. (in prep.).

6. Conclusions

In this paper, we present LOFAR detections of diffuse emission from 28 non-PSZ2 galaxy clusters that are in the LoTSS-DR2 sky coverage. In this sample, there are 13 radio halos (seven tentative detections), 14 relics (three tentative detections), five diffuse sources clearly associated with AGN remnants (four tentative detections), and 13 unclassified diffuse sources. We measure the flux densities and radio powers directly from the LOFAR maps. For radio halos, we fitted the SB with elliptical models and derive the flux densities from the best-fit model.

In our paper, we make several interesting points:

1. Diffuse sources are much harder to classify for lower mass clusters because ancillary radio and other data are sparser and the source sizes are smaller, making them harder to distinguish from other radio sources, such as AGN activity. For example, more than half of the halos in the sample are tentative detections.
2. A significant number of diffuse sources show an apparent connection to radio galaxies, as for example in WHL J002311.7+251510. There is also evidence for this at higher masses (e.g., van Weeren et al. 2021; Botteon et al. 2022) and it remains unclear as what role radio galaxies play in supplying relativistic electrons to the acceleration mechanisms that power diffuse radio sources, in particular radio relics. Our sample adds to the growing number of examples suggesting that there may be a causal connection between radio galaxies and certain types of relics. Follow-up work using surveys such as LoLSS (LOFAR LBA Sky Survey; De Gasperin et al. 2021), LoDeSS (LOFAR Decametre Sky Survey), and APERTIF (APERture Tile In Focus; Hess et al., in prep.) will be important for studying the spectral properties of halos and relics and to investigate the effects of AGN.
3. Radio halos in lower mass clusters are brighter than expected from the power–mass relation, although follow-up work is required before conclusions on the statistics of radio halos can be drawn. eROSITA (extended ROentgen Survey with an Imaging Telescope Array) surveys will provide a large X-ray-flux-limited sample of clusters and groups of galaxies that may help in testing scaling relations for diffuse radio sources (e.g., Pasini et al. 2021; Bulbul et al. 2022). A recent example of joint LOFAR and eROSITA observations of galaxy clusters is given by Ghirardini et al. (2021).

Acknowledgements. D.N.H., A.B., and E.B. acknowledge support from the ERC through the grant ERC-Stg DRANOEL n. 714245. M.B. acknowledges funding by the Deutsche Forschungsgemeinschaft (DFG, German Research Foundation) under Germany's Excellence Strategy – EXC 2121 'Quantum Universe' – 390833306. A.S. is supported by the Women In Science Excel (WISE) programme of the Netherlands Organisation for Scientific Research (NWO), and acknowledges the World Premier Research Center Initiative (WPI) and the Kavli IPMU for the continued hospitality. SRON Netherlands Institute for Space Research is supported financially by NWO. RJvW acknowledges support from the ERC Starting Grant ClusterWeb 804208. A.D. acknowledges support by the BMBF Verbundforschung under the grant 05A20STA. FG acknowledges support from INAF mainstream project 'Galaxy Clusters Science with LOFAR' 1.05.01.86.05. A.B. acknowledges support from the VIDI research programme with project number 639.042.729, which is financed by the Netherlands Organisation for Scientific Research (NWO). LOFAR (van Haarlem et al. 2013) is the Low Frequency Array designed and constructed by ASTRON. It has observing, data processing, and data storage facilities in several countries, which are owned by various parties (each with their own funding sources), and that are collectively operated by the ILT foundation under a joint scientific policy. The ILT resources have benefited from the following recent major funding sources: CNRS-INSU, Observatoire de Paris and Université d'Orléans, France; BMBF, MIWF-NRW, MPG, Germany; Science Foundation Ireland (SFI), Department of Business, Enterprise and Innovation (DBEI), Ireland; NWO, The Netherlands; The Science and Technology Facilities Council, UK; Ministry of Science and Higher Education, Poland; The Istituto Nazionale di Astrofisica (INAF), Italy. This research made use of the Dutch national e-infrastructure with support of the SURF Cooperative (e-infra 180169) and the LOFAR e-infra group. The Jülich LOFAR Long Term Archive and the German LOFAR network are both coordinated and operated by the Jülich Supercomputing Centre (JSC), and computing resources on the supercomputer JUWELS at JSC were provided by the Gauss Centre for Supercomputing e.V. (grant CHTB00) through the John von Neumann Institute for Computing (NIC). This research made use of the University of Hertfordshire high-performance computing facility and the LOFAR-UK computing facility located at the University of Hertfordshire and supported by STFC [ST/P000096/1], and of the Italian LOFAR IT computing infrastructure supported and operated by INAF, and by the Physics Department of Turin university (under an agreement with Consorzio Interuniversitario per la Fisica Spaziale) at the C3S Supercomputing Centre, Italy.

References

Abell, G. O., Corwin, H. G. Jr. , & Olowin, R. P. 1989, ApJS, 70, 1
Ackermann, M., Ajello, M., Albert, A., et al. 2016, ApJ, 819, 149
Alam, S., Albareti, F. D., Prieto, C. A., et al. 2015, ApJS, 219, 12
Aniyan, A. K., & Thorat, K. 2017, ApJS, 230, 20
Bagchi, J., Durret, F., Neto, G. B. L. G. B. L., & Paul, S. 2006, Science, 314, 791
Basu, K. 2012, MNRAS, 421, 1
Bender, A. N., Kennedy, J., Ade, P. A. R., et al. 2016, MNRAS, 460, 3432
Bernardi, G., Venturi, T., Cassano, R., et al. 2016, MNRAS, 456, 1259
Bonafede, A., Giovannini, G., Feretti, L., Govoni, F., & Murgia, M. 2009, A&A, 494, 429
Botteon, A., Cassano, R., Eckert, D., et al. 2019, A&A, 630, A77
Botteon, A., Giacintucci, S., Gastaldello, F., et al. 2021a, A&A, 649, A37
Botteon, A., Cassano, R., van Weeren, R. J., et al. 2021b, ApJ, 914, L29
Botteon, A., Shimwell, T. W., Cassano, R., et al. 2022, A&A, 660, A78
Boxelaar, J. M., van Weeren, R. J., & Botteon, A. 2021, Astron. Comp., 35, 100464
Brown, P. J., & Fuller, W. A. 1990, in Statistical Analysis of Measurement Error Models and Applications, (Providence, Rhode Island: American Mathematical Society), Contemporary Mathematics, 112
Brüggen, M., & Vazza, F. 2020, MNRAS, 493, 2306
Brunetti, G., & Jones, T. W. 2014, Int. J. Mod. Phys. D, 23, 1430007
Brunetti, G., & Lazarian, A. 2007, MNRAS, 378, 245
Brunetti, G., & Lazarian, A. 2011, MNRAS, 412, 817
Brunetti, G., Setti, G., Feretti, L., & Giovannini, G. 2001, MNRAS, 320, 365
Brunetti, G., Blasi, P., Cassano, R., & Gabici, S. 2004, MNRAS, 350, 1174
Brunetti, G., Giacintucci, S., Cassano, R., et al. 2008, Nature, 455, 944
Brunetti, G., Cassano, R., Dolag, K., & Setti, G. 2009, A&A, 507, 661
Brunetti, G., Blasi, P., Reimer, O., et al. 2012, MNRAS, 426, 956
Brunetti, G., Zimmer, S., & Zandanel, F. 2017, MNRAS, 472, 1506
Bulbul, E., Liu, A., Pasini, T., et al. 2022, A&A, 661, A10
Cassano, R., Ettori, S., Giacintucci, S., et al. 2010, ApJ, 721, L82
Cassano, R., Ettori, S., Brunetti, G., et al. 2013, ApJ, 777, 141
Cuciti, V., Cassano, R., Brunetti, G., et al. 2015, A&A, 580, A97
Cuciti, V., Cassano, R., Brunetti, G., et al. 2021, A&A, 647, A51
de Gasperin, F., Dijkema, T. J., Drabent, A., et al. 2019, A&A, 622, A5
de Gasperin, F., Rudnick, L., Finoguenov, A., et al. 2022, A&A, 659, A146
De Gasperin, F., Van Weeren, R. J., Brüggen, M., et al. 2014, MNRAS, 444, 3130
De Gasperin, F., Williams, W. L., Best, P., et al. 2021, A&A, 648, A104
Di Gennaro, G., van Weeren, R. J., Rudnick, L., et al. 2021, ApJ, 911, 3
Dwarakanath, K. S., Parekh, V., Kale, R., & George, L. T. 2018, MNRAS, 477, 957
Ensslin, T. A., Biermann, P. L., Klein, U., & Kohle, S. 1997, A&A, 409, 395
Fanti, C., Fanti, R., Feretti, L., et al. 1982, A&A, 105, 200
Feretti, L., Giovannini, G., Govoni, F., & Murgia, M. 2012, A&ARv, 20, 54
Gal, R. R., de Carvalho, R. R., Brunner, R., Odewahn, S. C., & Djorgovski, S. G. 2000, AJ, 120, 540
Ghirardini, V., Bulbul, E., Hoang, D. N., et al. 2021, A&A, 647, A4
Giacintucci, S., Venturi, T., Brunetti, G., et al. 2005, A&A, 440, 867
Giovannini, G., Bonafede, A., Feretti, L., et al. 2009, A&A, 507, 1257
Giovannini, G., Feretti, L., Girardi, M., et al. 2011, A&A, 530, L5
Govoni, F., Ferrari, C., Feretti, L., et al. 2012, A&A, 545, A74
Hardcastle, M. J., Shimwell, T. W., Tasse, C., et al. 2021, A&A, 648, A10
Hlavacek-Larrondo, J., Gendron-Marsolais, M.-L. L., Fecteau-Beaucage, D., et al. 2018, MNRAS, 475, 2743
Hoang, D. N., Shimwell, T. W., van Weeren, R. J., et al. 2018, MNRAS, 478, 2218
Hoang, D. N., Shimwell, T. W., van Weeren, R. J., et al. 2019, A&A, 622, A21
Hoang, D. N., Shimwell, T. W., Osinga, E., et al. 2021, MNRAS, 501, 576
Huber, P. J. 1981, Robust Statistics, Wiley Series in Probability and Statistics (Hoboken, NJ, USA: John Wiley & Sons, Inc.)
Jones, C., & Forman, W. 1999, ApJ, 511, 65
Jones, A., de Gasperin, F., Cuciti, V., et al. 2021, MNRAS, 505, 4762
Kale, R., Venturi, T., Giacintucci, S., et al. 2013, A&A, 557, A99
Kang, H., & Ryu, D. 2011, ApJ, 734, 18
Kang, H., Ryu, D., & Jones, T. W. 2012, ApJ, 756, 97
Kempner, J. C., & Sarazin, C. L. 2001, ApJ, 548, 639
Ledlow, M. J., Voges, W., Owen, F. N., & Burns, J. O. 2003, AJ, 126, 2740
Liang, H., Hunstead, R. W., Birkinshaw, M., & Andreani, P. 2000, ApJ, 544, 686
Lukic, V., Brüggen, M., Mingo, B., et al. 2019, MNRAS, 487, 1729
Markevitch, M., Govoni, F., Brunetti, G., & Jerius, D. 2005, ApJ, 627, 733
Murgia, M., Govoni, F., Markevitch, M., et al. 2009, A&A, 499, 679
Osinga, E., Van Weeren, R. J., Boxelaar, J. M., et al. 2021, A&A, 648, A11
Pasini, T., Brüggen, M., Hoang, D. N., et al. 2021, A&A, 661, A13
Pearce, C. J. J., van Weeren, R. J., Andrade-Santos, F., et al. 2017, ApJ, 845, 81
Petrosian, V. 2001, ApJ, 557, 560
Piffaretti, R., Arnaud, M., Pratt, G. W., Pointecouteau, E., & Melin, J.-B. B. 2011, A&A, 534, A109
Pinzke, A., Oh, S. P., & Pfrommer, C. 2017, MNRAS, 465, 4800
Planck Collaboration XXVII. 2016, A&A, 594, A27
Rajpurohit, K., Hoeft, M., Wittor, D., et al. 2021, A&A, 646, A135
Roettiger, K., Burns, J. O., & Stone, J. M. 1999, ApJ, 518, 603
Roger, R. S., Costain, C. H., & Bridle, A. H. 1973, AJ, 78, 1030
Rudnick, L., & Lemmerman, J. A. 2009, ApJ, 697, 1341
Scaife, A. M. M., & Heald, G. H. 2012, MNRAS, 423, 30
Sen, P. K. 1968, J. Am. Stat. Assoc., 63, 1379
Shimwell, T. W., Röttgering, H. J. A., Best, P. N., et al. 2017, A&A, 598, A104
Shimwell, T. W., Tasse, C., Hardcastle, M. J., et al. 2019, A&A, 622, A1
Shimwell, T. W., Hardcastle, M. J., Tasse, C., et al. 2022, A&A, 659, A1
Sommer, M. W., & Basu, K. 2014, MNRAS, 437, 2163
Strazzullo, V., Paolillo, M., Longo, G., et al. 2005, MNRAS, 359, 191
Struble, M. F., & Rood, H. J. 1999, ApJS, 125, 35
Tarrío, P., Melin, J.-B., & Arnaud, M. 2019, A&A, 626, A7
Tasse, C., Shimwell, T., Hardcastle, M. J., et al. 2021, A&A, 648, A1
Taylor, M. B. 2005, Astron. Data Anal. Softw. Syst. XIV - ASP Conf. Ser., 347, 29
van Weeren, R. J., Rottgering, H. J. A., Bruggen, M., & Hoeft, M. 2010, Science, 330, 347
van Weeren, R. J., Brüggen, M., Röttgering, H. J. A., et al. 2011, A&A, 533, A35
van Weeren, R. J., Brunetti, G., Brüggen, M., et al. 2016a, ApJ, 818, 204
van Weeren, R. J., Williams, W. L., Hardcastle, M. J., et al. 2016b, ApJS, 223, 2
van Weeren, R. J., de Gasperin, F., Akamatsu, H., et al. 2019, Space Sci. Rev., 215, 16
van Weeren, R. J., Shimwell, T. W., Botteon, A., et al. 2021, A&A, 651, A115
Vavilova, I. B., Dobrycheva, D. V., Vasylenko, M. Y., et al. 2021, A&A, 648, A122
Venturi, T., Bardelli, S., Dallacasa, D., et al. 2003, A&A, 402, 913
Venturi, T., Giacintucci, S., Dallacasa, D., et al. 2008, A&A, 484, 327
Wen, Z. L., & Han, J. L. 2015, ApJ, 807, 178
Wen, Z. L., Han, J. L., & Liu, F. S. 2012, ApJS, 199, 34
Williams, W. L., van Weeren, R. J., Röttgering, H. J. A., et al. 2016, MNRAS, 460, 2385
Wu, X.-P., Fang, L.-Z., & Xu, W. 1998, A&A, 338, 813
Zandanel, F., Pfrommer, C., & Prada, F. 2014, MNRAS, 438, 124
Zou, H., Gao, J., Xu, X., et al. 2021, ApJS, 253, 56

Appendix A: Halo model fitting

In Table A.1, we present the best-fit parameters obtained by the elliptical model for the candidate and detected radio halos. Details of the procedure are described in Sect. 3.4.

Table A.1. Best-fit parameters for the elliptical model.

Cluster	I_0 [μ Jy arcsec^{-2}]	x_0 [Deg]	y_0 [Deg]	$r1$ [kpc]	$r2$ [kpc]	ϕ [Deg]	$\chi^2_{\rm red}$
Abell 84	$1.0^{+0.1}_{-0.2}$	$10.4321^{+0.0050}_{-0.0047}$	$21.3776^{+0.0036}_{-0.0037}$	428^{+40}_{-44}	222^{+17}_{-18}	6^{+4}_{-4}	1.2
Abell 1330	$2.1^{+0.4}_{-0.6}$	$173.6790^{+0.0016}_{-0.0017}$	$49.4580^{+0.0018}_{-0.0017}$	163^{+25}_{-26}	81^{+17}_{-18}	125^{+9}_{-10}	1.2
MCXC J0928.6+3747	$9.9^{+0.2}_{-0.2}$	$142.1478^{+0.0002}_{-0.0002}$	$37.7854^{+0.0002}_{-0.0002}$	137^{+2}_{-2}	85^{+2}_{-2}	138^{+1}_{-1}	1.7
MCXC J0943.1+4659	$4.1^{+0.1}_{-0.1}$	$145.7555^{+0.0005}_{-0.0005}$	$46.9954^{+0.0005}_{-0.0005}$	340^{+10}_{-11}	298^{+9}_{-10}	126^{+9}_{-9}	1.2
PSZRX G100.21-30.38	$9.1^{+0.6}_{-0.7}$	$350.5652^{+0.0005}_{-0.0005}$	$28.5196^{+0.0005}_{-0.0005}$	29^{+13}_{-13}	132^{+10}_{-10}	39^{+8}_{-8}	1.6
PSZRX G102.17+48.88	$10.5^{+0.6}_{-0.6}$	$223.7549^{+0.0003}_{-0.0003}$	$62.9857^{+0.0003}_{-0.0003}$	100^{+5}_{-6}	67^{+4}_{-4}	55^{+5}_{-6}	1.2
PSZRX G195.91+62.83	$13.5^{+1.0}_{-1.0}$	$162.0197^{+0.0003}_{-0.0003}$	$31.6425^{+0.0003}_{-0.0003}$	110^{+7}_{-8}	79^{+6}_{-6}	37^{+8}_{-9}	0.7
WHL J130503.5+314255	$2.1^{+0.2}_{-0.2}$	$196.2459^{+0.0010}_{-0.0010}$	$31.7092^{+0.0011}_{-0.0012}$	252^{+23}_{-26}	212^{+22}_{-23}	98^{+28}_{-35}	0.8
WHL J165540.4+334422	$6.1^{+0.3}_{-0.3}$	$253.8812^{+0.0005}_{-0.0005}$	$33.7441^{+0.0005}_{-0.0005}$	159^{+8}_{-8}	115^{+5}_{-5}	63^{+6}_{-5}	1.3